

Dynamics of blue compact galaxies, as revealed by their H α velocity fields [★]

II. Mass models and the starburst triggering mechanism

Göran Östlin¹, Philippe Amram², Nils Bergvall³, Josefa Masegosa⁴, Jaques Boulesteix², and Isabel Márquez⁴

¹ Stockholm Observatory, SE-133 36 Saltsjöbaden, Sweden

² Laboratoire d'Astrophysique de Marseille, Observatoire de Marseille, 2 Place le Verrier, F-13248 Marseille Cedex 04, France

³ Astronomiska observatoriet, Box 515, S-75120 Uppsala, Sweden

⁴ Instituto de Astrofísica de Andalucía (CSIC), Apdo. 3004, E-18080 Granada, Spain

Received 15 January 2001, Accepted 17 May 2001

Abstract. The H α velocity fields of a sample of six luminous blue compact galaxies (BCGs) and two companions have been obtained by observations with a scanning Fabry-Perot interferometer. The Fabry-Perot images, velocity fields and rotations curves have been presented in a previous paper (Paper I). In general, the velocity fields are irregular and often contain secondary dynamical components, but display overall rotation. The two companions have more regular velocity fields and rotation curves. In this article we analyse the velocity fields and dynamics together with the morphology of the studied BCGs, and present detailed mass models. In addition, we model the stellar mass content by means of multicolour surface photometry and spectral evolutionary synthesis analysis. By comparison of the masses of stars and those derived from the rotation curve, we show that about half of the galaxies cannot be supported by rotation alone. The morphology and dynamics of the BCGs suggest that the starburst activity in these galaxies are most likely triggered by mergers involving gas-rich dwarf galaxies and/or massive gas clouds.

Key words. galaxies: compact – galaxies: starburst – galaxies: kinematics and dynamics – galaxies: evolution – galaxies: formation – galaxies: interactions

1. Introduction

The blue compact galaxies (BCGs) are characterised by their blue colour, strong nebular emission lines, compact appearance and low chemical abundances (e.g. Searle and Sargent 1972, Lequeux et al. 1979, Kunth and Sargent 1983; Masegosa et al. 1994, Izotov and Thuan 1999). The low chemical abundances and high star formation rates (SFRs) opened up the possibility that these were genuinely young galaxies presently forming their first generation of stars (Searle and Sargent 1972). Since these BCGs were found at low red-shift, this would mean that galaxies could still be forming in the local universe. If that would be the case, it would have considerable implications on theories on galaxy and structure formation, and on the nature of dark matter.

Since this was proposed, many BCGs have been found to contain a population of old stars. Evidence comes mainly from the studies of colours and morphologies of the faint halos seen around most BCGs (Loose and Thuan 1985; Kunth et al. 1988; Papaderos et al. 1996; Telles and Terlevich 1997; Doublier et al. 1999; Bergvall and Östlin 2000). Regular red halos are taken as evidence that there is an underlying old population present. Despite a few remaining young galaxy candidates it is evident that most BCGs are in fact old (see Kunth and Östlin 2000 for a review). What is less evident, however, is the reason why many BCGs seem to be forming stars at such high rates.

For many BCGs, the gas consumption time scales are significantly shorter than a Hubble time (e.g. Fanelli et al. 1988), which indicates that the current high SFRs have to be transient. The general picture has been that these galaxies undergo a few or several short bursts of star formation followed by longer more quiescent periods (Searle et al. 1973, Gerola et al. 1980). The explanation for this

Send offprint requests to: Göran Östlin, ostlin@astro.su.se

[★] Based on observations collected at the European Southern Observatory, La Silla, Chile;

could be gas dynamical; the gravitational field has to compete with galactic winds produced by mass loss and supernovae (SNe), which may expel the gas and prevent further star formation. Depending on the mass of the galaxy and the pressure in the surrounding intergalactic medium, the gas may cool and later accrete back on the galaxy producing a new burst (Babul and Rees 1992). It is believed though that the number of bursts has to be few, from gas consumption arguments and in order not to exceed the observed metallicities. However, the latter argument is not so strong in view of the possibility that BCGs lose enriched gas in supernovae winds created shortly after the onset of the starburst. On the other hand, as winds travel through the galaxy, the newly synthesised metals will mix with the surrounding ISM. Thus an outflow of gas is not necessarily more metal rich than the ISM in the galaxy (Ferrara and Tolstoy 2000).

Other explanations for the starburst phenomenon involve tidally triggered gas infall through interactions with companion galaxies (Lacey and Silk 1991). In this case one could imagine a disturbed gas-rich dwarf galaxy, or even an unevolved protogalactic cloud, as the progenitor of a BCG. However, some investigations show that most BCGs are fairly isolated: Campos-Aguilar et al. (1993) investigated the environments of HII-galaxies from the spectrophotometric catalogue by Terlevich et al. (1991) by comparing their location in space with those of galaxies in the CfA catalogue. They found that most HII-galaxies were isolated, and those that were not still had an average distance to its nearest neighbour of several hundreds of kpc. Similar results were obtained by Telles and Terlevich (1995). Salzer (1989) found that emission line galaxies were less clustered than normal giant galaxies and that they tended to avoid regions with high galactic density (of massive galaxies), similar to the results obtained for UV excess galaxies by Iovino et al. (1986), and recently by Telles & Maddox (2000).

On the other hand, Taylor et al. (1995, 1996a, erratum 1996b; Taylor 1997) made HI surveys for companion galaxies around HII-galaxies and LSBGs. They found that nearly 60% of the HII-galaxies in their sample had HI companions. The important difference with respect to the studies above is that this survey was a direct search sensitive also to faint gas-rich dwarf galaxies, while the others used catalogues with bad completeness for dwarfs. Thus, while BCGs tend to avoid giant luminous galaxies, they appear to have dim low-mass neighbours in many cases.

In any case, it is likely that the BCGs hold some key information about the early evolution and formation of dwarf and intermediate sized galaxies. If it can be understood how BCGs evolve on a longer time scale and under what circumstances an 'object' can be transformed into a BCG, much will have been learned about the evolution of galaxies. Some have proposed a relationship with faint blue galaxies (FBGs) at $z \sim 0.5$ (Cowie et al. 1991; Babul and Rees 1992), others with low surface brightness galaxies (LSBGs), which may be the precursors and/or the successors of BCGs (Bergvall et al. 1999a, 1999b; Telles and

Terlevich 1997). Further, an understanding of BCGs may help in interpreting observations of star forming objects at high red-shifts. The studies of intermediate-high red-shift compact galaxies in the Hubble deep field (Guzmán et al. 1996, 1997; Phillips et al. 1997) reveal that these include galaxies with properties very similar to those of local luminous BCGs.

Fully understanding the evolution of BCGs requires detailed knowledge about their star formation histories (SFHs), dynamics, and possible merger history. Most BCGs are far too distant to be resolved into stars even with the Hubble Space Telescope (HST). Instead, the SFHs can be examined with the help of spectral evolutionary synthesis models (SEMs) and optical surface photometry (Östlin and Bergvall 1994, Östlin et al. 1996, Bergvall and Östlin 2000). This can put constraints both on star formation processes, including the initial mass function (IMF) of stars and the number of old stars present. The tricky part is to constrain the mass of the old, cool stellar component, since the light in the optical is totally dominated by hot/massive stars. The old population is easier approached in the halos, outside the starburst region, and by adding observations in the near infrared (NIR) (Bergvall and Östlin 2000). A lot could also be gained with knowledge of the dynamics of BCGs, from which one can then put interesting constraints on the amount of old stars and dark matter present, and provide important information on the triggering mechanism behind starbursts in BCGs.

Previous studies of the dynamics of BCGs include optical and radio investigations. The latter target the 21cm emission from neutral hydrogen and is very useful for studying the large scale dynamics, while the inferior spatial resolution (as compared to the optical regime) make them of limited use for studying the central dynamics and the kinematics of the star forming regions. Optical studies have probed either the full two dimensional velocity field, e.g. by utilising Fabry-Perot interferometry (Thuan et al. 1987, Marlowe et al. 1995, Petrosian et al. 1997, Östlin et al. 1999) or limited parts from slit spectroscopy (e.g. Gil de Paz et al. 1999). The general picture is that of large scale rotation (Östlin et al. 1999) and smaller scale distortions e.g. in the form of expanding bubbles (Marlowe et al. 1995, Martin 1998, Kunth et al. 1998, Östlin et al. 1999, Gil de Paz et al. 1999). Radio observations provide further evidence for large scale rotation in BCGs (Viallefond et al. 1987; Bergvall and Jörsäter 1988; Meurer et al. 1996, 1998; van Zee et al. 1998).

The notion "starburst" is frequently used in the literature to describe galaxies, or regions of galaxies, with varying degrees of star formation activity. In this paper, we will adopt a more strict definition by requiring that a starburst involves a global SFR which is unsustainably high. The SFR may be unsustainable because the gas consumption time scale, or the time scale to build up the observed stellar mass, is significantly shorter than the Hubble time, i.e. the time averaged SFR is an order of magnitude lower than the present. Many galaxies have SFRs fluctuating

with time, and/or have impressive bright HII regions, but this does not necessarily imply that the SFR is unsustainable over a Hubble time. Indeed, many galaxies classified as BCGs in the literature are *not* starburst according to our definition.

1.1. Sample selection and Fabry-Perot observations

In this paper we will discuss the results from a study of the dynamics of BCGs. In 1995, we obtained Fabry-Perot interferometric observations, targeting the H α emission line, for a sample of six luminous BCGs ($M_B \in [-17, -20]$) and two companion galaxies. Four of the BCGs were taken from the catalogue of compact galaxies by Bergvall and Olofsson (1986). One galaxy (ESO 185-13) was taken from an extension of this catalogue (Bergvall et al. unpublished). The last BCG (Tololo 0341-407) was taken from the spectrophotometric catalogue of HII galaxies by Terlevich et al. (1991). The galaxies were selected to be actively star forming, as judged by the equivalent width and luminosity of H β or H α . The four galaxies from the Bergvall and Olofsson (1986) catalogue are the ones with the highest the equivalent widths in H β from that list. The two other BCGs were in addition chosen because they had the right coordinates with respect to the allocated observing time. The reason for choosing intrinsically luminous BCGs was to get a more homogeneous sample, in view of the fairly small number of galaxies observed. Two of the BCGs selected from the Bergvall and Olofsson (1986) catalogue have confirmed physical star forming companions, and these were also included in the target list.

The observations and reductions are thoroughly described in Paper I (Östlin et al. 1999, hereafter Paper I), where we also present the velocity fields, rotation curves and rough mass estimates. The velocity fields obtained appear to be very peculiar, showing non axi-symmetric distortions and in several cases evidence for multiple dynamical components. In this paper we will continue the discussion and combine the dynamics with surface photometric data to model the dynamical and photometric masses of the galaxies. Moreover, morphologies will be discussed in detail.

The absolute visual magnitudes of BCGs range from -12 to -21 , and there is of course no guarantee that our sample of relatively luminous BCGs is representative for all BCGs. Nor is there any guarantee that BCGs with similar mass or luminosity have similar physical origin. Morphologically there exist different types of BCGs (Loose and Thuan 1985, Salzer et al. 1989, Kunth et al. 1988, Telles et al. 1997). Apart from the varying intrinsic luminosities, the relative intensity of star formation varies as well and not all BCGs are starbursts. Many BCGs are simply distant dwarf irregulars with moderately active star formation that have been picked up in emission line surveys. Telles et al. (1997) found that BCGs which have irregular morphology at faint isophotal levels, are on average more luminous than those with regular morphology.

Most of the BCGs in our sample have irregular morphology and thus may have a physically different evolutionary history as compared to low mass BCGs with regular morphology.

In 1999 and 2000 we carried out observations of some 15 new BCGs at La Silla, extending our sample to lower luminosities, and observing time for spectroscopic and photometric followup has been obtained. The new sample was selected to extend our luminosity range downwards, and include galaxies with a minimum H β equivalent width (sometimes estimated from H α) of ~ 30 Ångström. These observations will be discussed in forthcoming papers. In addition, we obtained complimentary observations of the H α line widths for the BCGs in the current sample, which will be partly used in the present paper.

Throughout the paper we use $H_0 = h_{75} \cdot 75$ km/s/Mpc, with $h_{75} = 1$. In general, absolute photometric properties like masses, luminosities and SFR, scale with h_{75}^{-2} . Kinematical properties are not sensitive to the choice of h_{75} , but the kinematical mass estimates scale with h_{75}^{-1} since they involves a length scale. Relative properties like mass to light ratios and time-scales do not depend on h_{75} .

2. Photometric data and analysis

In this section we will describe the photometric data available and how we use this to obtain realistic estimates of the mass of the stellar populations in the target galaxies.

2.1. Photometric data and decomposition

For most of the galaxies we have extensive optical and near infrared images and, in addition, photo-electric photometry (Bergvall and Olofsson 1986; Bergvall and Olofsson private correspondence). These data have been collected at the ESO telescopes on La Silla. The available photometry for each galaxy is shown in Table 2.

The luminosity profiles have been derived by integrating in elliptical rings, using the same position angle and inclination as derived from the kinematical data. The luminosity profile software was written in Uppsala and is described in Bergvall and Östlin (2000), where the photometric properties of several of the galaxies in the present study is discussed at length.¹

The luminosity profile of a galaxy traces the spatial distribution of its stars. In the ideal case of a uniform stellar population with no extinction, the surface brightness directly reveals the stellar mass density. However if the mass to luminosity ratio of the stellar population varies, e.g. due to star formation, there will be no simple relation between the observed luminosity distribution and the real mass distribution of stars.

¹ Note that the luminosity profiles used in this paper and those presented in Bergvall and Östlin (2000) may differ slightly due to slightly different choices of inclination and position angle for the ellipses. However, this does not affect the relative contribution of the two components, and hence not the photometric mass estimates below.

In BCGs this problem is serious because, in general, the starburst population dominates the emission of light, but not the mass. Furthermore, since the fraction of old stars is a priori unknown (especially in the starburst region) and the starburst has a rapid luminosity evolution, the mass to light ratio of the stellar population is very uncertain and varies with galacto-centric distance. In general, the starburst region is close to the optical centre of a BCG. In the outskirts M/L may be above one, while in the youngest region of the burst it should be much lower. To make progress we have taken the following approach:

By looking at the radial colour profiles, we determine the extent of the starburst. In the outskirts the colours are stable (see Fig. 1), indicating that the assumption of a homogeneous stellar population is plausible here. Therefore, the luminosity profile of each galaxy was decomposed into two components, a *disk* and a *burst*. The disk component has little or no colour gradient and is interpreted as the underlying, older, population. It has been produced from an exponential fit to the luminosity profile (usually in the V-band) at radii where the colours were stable, and, if possible, comparable to the radius of the last measured point in the rotation curves. In all cases, an exponential law provides a good fit to the data at these radii. The residual after subtracting the disk component, we call the burst component. The true photometric structure of the galaxies at larger radii may be more complicated (Bergvall and Östlin 2000), but this is not of concern here since we are only interested in estimating the mass of the stellar population within the extent of the rotation curves. An example of the photometric decomposition is shown in Fig. 1. Note how the colours stabilise at the same radius as the disk takes over from the burst as the main contributor to the emitted light. This is the typical situation in the sample studied here. A representative choice of colour indices for the disk and the subtracted burst components are shown in Table 2. Multi-wavelength colour profiles for all galaxies, except ESO 185-13 and Tololo 0341-407, are presented in Bergvall and Östlin (2000).

2.2. Internal extinction

BCGs in general have low internal extinction (e.g. Mas-Hesse and Kunth 1999), which probably is a consequence of low chemical abundances and selection criteria that favour galaxies with blue colours. The central $E(B - V)$ values derived spectroscopic observations of the $H\alpha/H\beta$ ratio and Case B recombination are given in Table 2. In some cases, these could be overestimated due to underlying Balmer absorption from young A-type and old stars. Long slit spectra (Bergvall and Östlin 2000) indicate that the $H\alpha/H\beta$ ratio decreases with radius. Moreover, investigations including the UV-continuum suggest that the emission lines are more heavily reddened than the stellar continuum (Calzetti et al. 1994; Mas-Hesse and Kunth 1999). Hence, applying the $E(B - V)$ values in Table 2 throughout would overestimate the internal extinction.

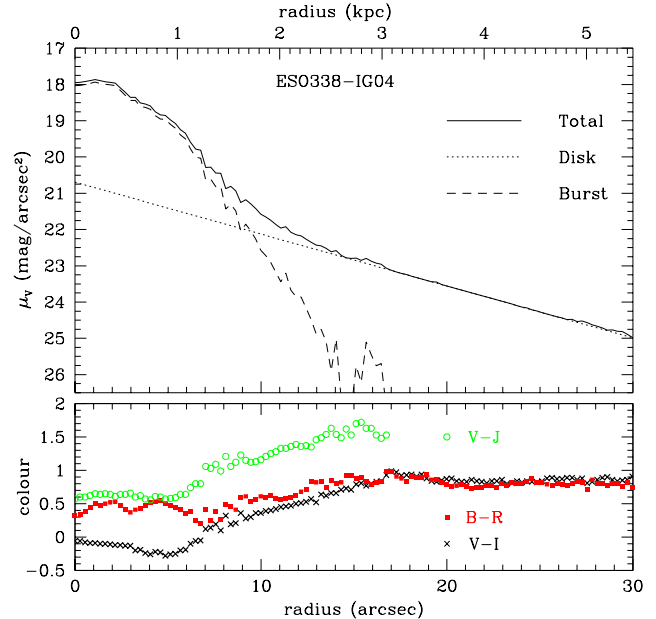


Fig. 1. Radial luminosity and colour profiles for ESO 338-IG04. The upper panel shows the V-band surface brightness (uncorrected for inclination): The total luminosity profile is shown as a solid line, the fitted disk component is shown as dotted line, and the burst component is shown as a dashed line. The lower panel shows the radial $V - J$, $B - R$, and $V - I$ colour profiles, where B , V and J are in the Johnson system, and R and I in the Cousins system. The optical and the near infrared data has been obtained at La Silla with NTT+EMMI and 2.2m+IRAC2, respectively (see Bergvall and Östlin 2000).

We have used the values given in Table 2 for the central of the galaxies and assumed that the extinction coefficient scales with the thickness of the disk, i.e. the surface brightness. In effect, the adopted extinction for the burst component is close to the values given in Table 2, whereas the extinction for the disk component is significantly smaller. In any case, the reddenings in Table 2 are small and the uncertainty in the disk $E(B - V)$ values do not seriously affect the derived photometric masses, as we argue below.

2.3. Spectral evolutionary synthesis models

We use a spectral evolutionary synthesis model in combination with colour profiles in the optical and near infrared to estimate the mass-to-light ratios of the galaxies. The model used has been developed by Bergvall and is described in Bergvall and Rönnback (1995), Östlin et al. (1998) and Bergvall and Östlin (2000). Briefly, it is based on stellar evolutionary tracks from the Geneva group (Schaller et al. 1992), mostly Kurucz (1992) model atmospheres, and a nebular emission component from Cloudy (Ferland 1993). Moreover, pre-main sequence stage evolution from VandenBerg (1985; private correspondence

Table 1. Spectral evolutionary synthesis model parameters used in M/L determinations. The IMF slope is defined as $dN/dM \propto M^{-\alpha}$, where M is the stellar mass and dN is the number of stars in the mass interval $[M, M + dM]$. The classical value by Salpeter (1955) is $\alpha = 2.35$.

IMF slope α	2.0, 2.35 and 2.70
Lower mass limit M_{low}	0.1 and 1.0 M_{\odot}
Upper mass limit M_{up}	30 and 100 M_{\odot}
Burst duration τ	50 and 16000 Myr
SFR e-folding time β	0 and 3 Gyr
Metallicity	0.1 Z_{\odot}

1986), and horizontal branch and AGB stages up to the onset of thermal pulsations from Castellani et al. (1991), have been included. Empirical data are used to extend the evolution to the tip of the AGB. Most of the galaxies have determined nebular oxygen abundances, which are close to 1/10th of solar (Bergvall and Östlin 2000; Masegosa et al. 1994). This value was therefore used for the stellar and gaseous components in the spectral evolutionary synthesis model. The used model parameters are summarised in Table 1.

The model also calculates M/L_V , the V-band mass to light ratio for the stellar population. This includes the mass of stellar remnants, and the gas returned to the interstellar medium. Counting only the mass of stars and remnants would result in slightly lower M/L values. What matters is to what extent the returned gas is used for new star formation. Since these galaxies have low metallicity their ISM are not heavily polluted and the returned gas will be diluted before any of it is taken up in new stars. Hence it is justified to include the returned gas in the mass budget for calculating M/L .

The models by Bergvall, described in Table 1, were complimented with models produced with the PEGASE.2 code (Fioc and Rocca-Volmerange 1999), to check consistency and to further explore the parameter space. In particular, models with shorter star formation time-scales (instantaneous burst and e-folding times of 10, 30 and 100 Myr) were used to constrain the properties of the central “burst” regions.

2.4. M/L values

The ensemble of model predictions characterised in Table 1 were compared to the observed broad-band colours of the galaxies. The colours of the disk and burst components were modelled separately. Taking the observational uncertainties into account, we determine which models reproduce the disk colours within $\sim 3\sigma$ and read off their M/L value. Some models were discarded because they give unreasonable M/L values at certain ages, e.g. short burst models with lower mass limit $M_{\text{low}} = 1M_{\odot}$ and ages larger than a few Gyr. Such models are in any case not very re-

alistic. Apart from this, the best-fitting M/L is generally well defined, as is also the minimum allowed M/L value. The upper limit to the M/L value is generally less well constrained.

In many cases there is a “good degeneracy”, in the sense that while the best fitting age is sensitive to the choice of model parameters, the corresponding M/L values are very similar. We illustrate this with the following example: Compared to a standard $\alpha = 2.35$ model, a model with a steeper $\alpha = 2.85$ IMF, will for each time-step have redder colours and higher M/L . Fitting a galaxy’s colour to this steep IMF model will produce a lower age, and this will to first order compensate for the change in M/L . The same effect occurs if one varies the metallicity. Similarly, increasing the assumed $E(B - V)$ value decreases the modelled age and M/L but this effect is to a first order compensated by the increasing amount of absorbed emission to correct for.

In this paper, we have only considered single power-law IMFs. The use of broken power-law IMFs with two or more segments (e.g. Miller & Scalo 1982, Kroupa et al. 1993, Scalo 1986, 1998) could decrease the modelled M/L values somewhat, up to a factor of 2 at large ages. Hence, if the IMF in our galaxies has a flatter low mass range, the real M/L values would approach the lower limits given in Table 2. On the other hand, the possible extension of the IMF to objects with sub-stellar masses would increase M/L by $\sim 10\%$ for an IMF with relatively flat slope in the regime below 1 M_{\odot} .

In general, models with $M_{\text{low}} = 0.1 M_{\odot}$, $M_{\text{up}} = 100 M_{\odot}$, $\alpha = 2.35$ and a continuous but exponentially decaying ($\beta = 3$ Gyr) star formation rate give the best fit to the observed colours of the disk component. The best fitting ages are found between 2.5 and 8 Gyr for the different galaxies (between 1 and 16 Gyr considering the lower and upper 3σ limits). Of course there might be even older components present, that however cannot make a significant contribution to the mass within the modelled radii. The age of the halo stellar populations is further discussed in Bergvall and Östlin (2000). The resulting M/L values for the disk component are shown in Table 2. For ESO 185-13, we have only optical surface photometry in V and R and no near-IR data and consequently its M/L_{disk} values are less certain. For one galaxy (Tololo 0341-407), we did not have multicolour data, and instead we used the median value M/L_{disk} for the other galaxies, and the extreme of $M/L_{\text{disk}}^{\text{min}}$ and $M/L_{\text{disk}}^{\text{max}}$ for the allowed range; these values are flagged with a colon (:) in Table 2.

It was more difficult to constrain the M/L values for the burst components, since there is a large dependence on model parameters and strong colour gradients. Moreover, ionised gas emission is important and may be non-local, i.e. the emitting gas is displaced with respect to the ionising source and e.g. found in filaments (Östlin et al. 1998). The contribution of line and continuous emission from ionised gas has the effect of making the burst colours presented in Table 2 redder. Part of the difficulty may arise because the burst population is not completely

Table 2. Available photometry and adopted V-band M/L ratios:

Galaxy (1)	$E(B - V)$ (2)	Photometry (3)	Disk/Burst colours (4)	Disk colour (5)	M/L_{disk} (6)	$M/L_{\text{disk}}^{\text{min}}$ (7)	$M/L_{\text{disk}}^{\text{max}}$ (8)	M/L_{burst} (9)
ESO 350-38	≤ 0.25	<i>BVRIJHK</i>	$B - V = 0.5/0.3$	$V - J = 1.9$	3.0	2.0	6.0	0.05
ESO 480-12	≤ 0.30	<i>BVRIJHK</i>	$B - V = 0.3/0.0$	$V - J = 1.6$	2.3	1.6	3.6	0.06
ESO 338-04	≤ 0.06	<i>BVRIJHK</i>	$B - V = 0.3/0.2$	$V - J = 1.7$	3.0	2.1	3.8	0.05
ESO 338-04B	≤ 0.06 :	<i>VIJHK</i>	$V - I = 0.7/0.0$	$V - J = 1.6$	3.4	2.5	6.0	0.10
ESO 185-13	≤ 0.16	$U^a B^a VRI^a$	$V - R = 0.4/0.2$		2.2	1.0	6.0	0.08
ESO 400-43	≤ 0.22	<i>BVRIJHK</i>	$B - V = 0.9/ - 0.2$	$V - J = 1.6$	3.1	2.2	6.5	0.06
ESO 400-43B	≤ 0.17	$BV^a RI^a JHK$	$B - R = 0.8/0.4$	$B - J = 2.3$	3.0	1.0	4.0	0.10
Tol 0341-403E	≤ 0.24	<i>R</i>			3.0:	1.0:	6.0:	0.03
Tol 0341-403W	≤ 0.29	<i>R</i>			3.0:	1.0:	6.0:	0.05

Description of column contents: (1) Name of galaxy. (2) The central $E(B - V)$ derived from spectroscopy. The source is Bergvall and Östlin (2000), except for ESO 185-13 (Calzetti et al. 1994) and Tololo 0341-403 (Terlevich et al. 1991). For E338-04B no spectroscopic $E(B - V)$ was available and we used the same value as for ESO 338-04, and flagged it with a colon (:). (3) Available photometry. Entries with superscript ^a indicates that for this filter only aperture photometry is available. (4) Representative optical colours for the disk and burst regions, corrected for extinction (see Sect. 2.2). B and V are in the Johnson filter system, R and I in the Kron-Cousins filter system. Typical errors are 0.1 or less for the disk, and slightly larger for the burst components. (5) Representative optical-near infrared colour for the disk components, errors 0.2-0.3. (6) shows the best fitting M/L_V values (in solar units) for the disk component. (7) and (8) show the 3σ upper and lower limits on the disk M/L_V , respectively. The uncertain M/L_V values for Tololo 0341-403 are indicated with colon, see text for further explanation. (9) Best fitting M/L_V estimate for the burst component.

coeval, but includes a mix of stars with ages differing up to several 10 Myrs. For the burst, we used also the observed $H\alpha$ equivalent-widths to constrain its age and M/L . We were able to constrain that in all cases $0.01 < M/L < 0.2$, except when using a very steep IMF ($\alpha \geq 3.0$), which however gives worse fits to the data. We have used the values given in Table 2 as our estimates for the burst, with a generous allowed interval of $M/L = 0.01$ to $M/L = 0.4$, common for all galaxies. Within this range in M/L , the burst always make a minor contribution to the total photometric mass.

2.5. Star formation rates and time-scales

With the aid of the spectral synthesis code described in Sect. 2.2., the integrated $H\alpha$ luminosities have been used to derive the total star formation rates in the observed galaxies. For a Salpeter IMF with mass range $0.1 - 100 M_\odot$, and with $L(H\alpha)$ in Watts, the SFR expressed in M_\odot/yr is:

$$SFR = L(H\alpha)/1.51 \cdot 10^{34}$$

The integrated SFR for all galaxies are given in Table 4; the $H\alpha$ luminosities are given in Table 5 in Paper I. Note that these are lower limits since the $H\alpha$ luminosities were derived assuming no extinction. In addition, some of the very youngest star forming regions may be completely embedded. The central $E(B - V)$ estimates, derived from from spectroscopic $H\alpha/H\beta$ values, are in the range $E(B - V) = 0 - 0.3$, corresponding to correction factors of 1.0 to

2.0 for $L(H\alpha)$. However, slit spectra indicate that $H\alpha/H\beta$ decrease outside the centre, and since we do not know the “global” $E(B - V)$ values we did not apply any correction to the values in Table 4. The derived star formation rates span 1 to 20 M_\odot per year for the BCGs, whereas the companion to ESO 338-IG04 has a lower SFR.

Together with the photometric and rotational mass estimates the integrated SFR estimates can be used to derive mass averaged values. In Table 4 we give the SFR normalised to the photometric galaxy masses. The normalisation using rotational mass would in some cases (when there is an apparent dynamical mass deficiency) overestimate the mass averaged SFR, and this quantity is not presented explicitly.

The inverse of the mass averaged SFRs also provide τ_{ph} , the time scale for building up the observed photometric mass in stars with the current SFR. In general, τ_{ph} is close to 1 Gyr, meaning that the current SFR is one order of magnitude larger than the average past SFR. Thus, these galaxies are true star bursts in the sense that their SFR is an order of magnitude higher than what is sustainable over a Hubble time. Note that the modelling in Sect. 2.3 indicate ages of several Gyrs for the underlying populations. For the two companions we find larger values of τ_{ph} . In the eastern component of Tololo 0341-407 $\tau_{\text{ph}} \sim 0.25$ Gyr, indicating a momentary very enhanced SFR, although its photometric mass is quite uncertain.

Similarly, we can define $\tau_b = M_{\text{burst}}/SFR$, the time scale for building up the observed burst mass. Hence τ_b gives an order of magnitude estimate of how long the present burst has been active. Values of τ_b are given in

Table 3. Absolute magnitudes, and mass estimates of disk and burst components.

Galaxy	R	Disk	Burst	M_{disk}	M_{burst}	M_{ph}	M_{rot}	Note
(1)	kpc	M_V	M_V	$10^9 M_\odot$	$10^9 M_\odot$	$10^9 M_\odot$	$10^9 M_\odot$	(9)
(1)	(2)	(3)	(4)	(5)	(6)	(7)	(8)	(9)
ESO 350-IG38	6.0	-19.3	-20.4	$13^{+13}_{-4.4}$	$0.64^{+4.5}_{-0.51}$	$13.9^{+18}_{-4.9}$	$0.87^{+2.1}_{-0.60}$	Rmax, non decomp.
“	0.4	-15.8	-15.4	$0.51^{+0.51}_{-0.17}$	$0.006^{+0.050}_{-0.005}$	$0.52^{+0.56}_{-0.18}$	$0.60^{+0.90}_{-0.40}$	Vmax, non decomp.
“	5.2	-19.2	-20.4	$13^{+13}_{-4.2}$	$0.64^{+4.5}_{-0.52}$	$13^{+17}_{-4.7}$	$1.6^{+3.2}_{-1.1}$	DVF: 1st comp.
“	1.0	-17.3	-18.1	$2.1^{+2.1}_{-0.7}$	$0.078^{+0.54}_{-0.062}$	$2.1^{+2.6}_{-0.75}$	$1.3^{+5.6}_{-0.90}$	DVF: 2nd comp.
ESO 480-IG12	5.9	-18.4	-19.2	$4.6^{+2.6}_{-1.4}$	$0.25^{+1.4}_{-0.21}$	$4.8^{+4.0}_{-1.6}$	$17^{+17}_{-8.2}$	Rmax
ESO 338-IG04	2.5	-17.3	-19.0	$2.2^{+0.58}_{-0.65}$	$0.17^{+1.2}_{-0.14}$	$2.3^{+1.8}_{-0.80}$	$0.57^{+1.8}_{-0.50}$	masked Rmax
“	1.9	-17.0	-19.0	$1.6^{+0.4}_{-0.5}$	$0.17^{+1.2}_{-0.14}$	$1.8^{+1.6}_{-0.62}$	$0.86^{+2.0}_{-0.70}$	masked Vmax
ESO 338-IG04B	3.6	-17.7	-16.4	$2.8^{+2.2}_{-0.75}$	$0.032^{+0.10}_{-0.03}$	$2.9^{+2.3}_{-0.78}$	$5.7^{+6.0}_{-2.9}$	Rmax
ESO 185-IG13	3.8	-18.7	-18.7	$5.6^{+9.7}_{-3.1}$	$0.21^{+0.85}_{-0.18}$	$5.8^{+11}_{-3.3}$	$1.5^{+1.9}_{-0.90}$	Rmax
ESO 400-G43	10.9	-19.2	-20.0	$12^{+13}_{-3.4}$	$0.52^{+2.9}_{-0.43}$	$12^{+16}_{-3.9}$	$0.29^{+0.70}_{-0.20}$	Rmax
“	5.7	-18.9	-20.0	$9.9^{+11}_{-2.9}$	$0.50^{+2.9}_{-0.42}$	$10^{+14}_{-3.3}$	$0.66^{+1.1}_{-0.50}$	Both
“	1.1	-16.9	-18.2	$1.6^{+1.7}_{-0.46}$	$0.094^{+0.53}_{-0.078}$	$1.7^{+2.3}_{-0.54}$	$0.60^{+0.70}_{-0.30}$	Vmax
ESO 400-G43B	4.8	-17.9	-18.1	$3.6^{+1.2}_{-2.4}$	$0.15^{+0.46}_{-0.14}$	$3.8^{+1.7}_{-2.6}$	$3.3^{+2.1}_{-1.5}$	Rmax
Tololo 0341-403E	1.6	-14.6	-15.9	$0.17^{+0.17}_{-0.12}$	$0.006^{+0.073}_{-0.004}$	$0.18^{+0.25}_{-0.12}$	$0.17^{+0.5}_{-0.1}$	Both
Tololo 0341-403W	1.9	-15.6	-16.5	$0.43^{+0.43}_{-0.29}$	$0.018^{+0.12}_{-0.014}$	$0.45^{+0.56}_{-0.30}$	$0.26^{+0.50}_{-0.20}$	Both

Description of column contents: (1) Name of galaxy (2) Radius (in kpc) within which the properties in columns 3 to 8 have been evaluated. (3) Absolute V-band magnitude of disk component. (4) Absolute V-band magnitude of burst component. (5) Estimated photometric mass of the disk component. (6) Estimated photometric mass of the burst component. (7) Total photometric mass of the disk+burst component. (8) Rotational mass. The quoted uncertainties reflect the uncertainty in: the parameter f , the inclination and the rotational velocity, see Paper I. (9) Comments: For some galaxies we present mass estimates at more than one radii, corresponding to certain features in the rotation curve (see Paper I). “Rmax” and “Vmax” means that the mass was evaluated at the last measured point in the rotation curve, and at the radius of maximum velocity, respectively. “Both” means that the mass was evaluated at the last point where both the approaching and receding sides could be measured. For ESO 350-38 we present mass estimates obtained both from the model decomposing the velocity field into two dynamical components (DVF) and for the “raw” velocity field. For ESO 338-04 some points in the velocity field had to be masked in order to at all be able to derive a rotation curve. NB: For all entries, the quoted uncertainties represent the maximum expected deviation, i.e. rather 3-sigma than 1-sigma deviations.

Table 4. If the SFR has passed its peak, τ_b will overestimate the burst duration. In ESO 338-IG04 we find $\tau_b \sim 50$ Myr, in good agreement with the burst duration derived from the age distribution of young star clusters resolved with the HST (Östlin et al. 1998).

Since we corrected for extinction in deriving $M_{ph,26}$ and M_{burst} , but not when deriving the SFR, the timescales τ_{ph} and τ_b may be slightly overestimated, by up to a factor of two.

Another time scale can be constructed for those galaxies where the HI content is known, i.e. the gas consumption time scale. All galaxies in the sample have determined HI-masses or upper limits. The gas consumption time scale ranges from the extreme value of 5 Myr (sic) for ESO 350-IG38 (which has an upper limit of $M_{HI} < 10^8 M_\odot$, but see Sect. 4.1) to ~ 3 Gyr for the companion of ESO 400-G43. All BCGs have gas consumption time-scales smaller than 1 Gyr, showing that the present SFRs are unsustainable.

Table 4. Derived global properties.

Galaxy	SFR M_{\odot}/yr	$M_{\text{ph},26}$ $10^9 M_{\odot}$	M/L_{26}	$SFR/M_{\text{ph},26}$ 10^{-9} yr^{-1}	τ_{ph} Gyr	τ_{b} Myr	$r_{\text{e,d}}$ kpc	σ km/s	M_{σ} $10^9 M_{\odot}$
(1)	(2)	(3)	(4)	(5)	(6)	(7)	(8)	(9)	(10)
ESO 350-IG38	18.5	15.5	0.87	1.19	0.84	34	2.6	81	18.8
ESO 480-IG12	4.1	5.3	0.83	0.77	1.29	60	2.6	51	7.7
ESO 338-IG04	3.2	4.0	0.85	0.80	1.24	53	2.2	43	4.6
ESO 338-IG04B	0.3	3.2	2.53	0.08	12.1	120	1.7	29	1.6
ESO 185-IG13	5.4	7.1	1.21	0.76	1.32	40	2.0	40	3.7
ESO 400-G43	11.3	12.7	1.07	0.89	1.12	45	3.1	49	8.3
ESO 400-G43B	1.3	4.9	1.52	0.27	3.70	110	2.6	34	3.4
Tololo 0341-403E	1.3	0.3	0.98	4.38	0.23	5	1.6	34	2.1
Tololo 0341-403W	0.9	1.0	1.43	0.90	1.11	19	2.2	36	3.3

Description of column contents: (1) Name of galaxy. (2) Star formation rate (SFR) derived from the integrated $\text{H}\alpha$ luminosity, uncorrected for internal extinction. (3) Integrated (disk+burst) photometric mass within the $\mu_V = 26 \text{ mag/arcsec}^2$ isophote. (4) Integrated V-band mass to light ratio within $\mu_V = 26 \text{ mag/arcsec}^2$. (5) SFR per unit (photometric) mass of the galaxy. (6) Inverse of $SFR/M_{\text{ph},26}$, giving the time-scale for building up $M_{\text{ph},26}$ with the current SFR. (7) Time scale for accumulating the observed burst mass with current SFR. (8) Effective (half-light) radius of the disk component. (9) Integrated $\text{H}\alpha$ line-width. (10) Mass inferred from the $\text{H}\alpha$ line-width.

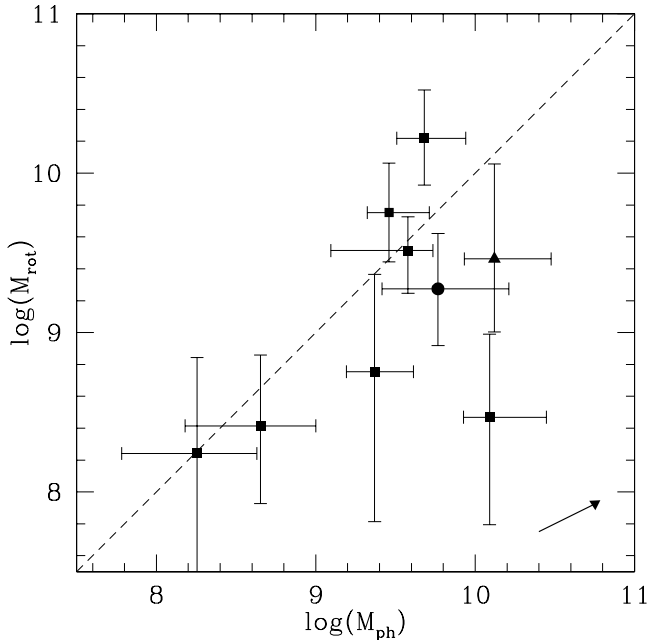


Fig. 2. Comparison of the photometric and dynamical (rotational) masses. The X-axis shows the logarithm (base 10) of the derived photometric mass in units of M_{\odot} . The Y-axis shows the logarithm of the rotational mass. The data-points are taken from Table 3, except for ESO 350-38 (filled triangle) and ESO 185-13 (filled circle), where M_{rot} is the sum of the rotational masses of the two distinct components in the velocity field (see Paper I). The diagonal dashed line shows the location of galaxies for which the photometric and rotational masses are equal. The arrow in the lower right shows the effect of going from $H_0 = 75$ to 50 km/s/Mpc .

2.6. Photometric mass estimates, and comparison with rotational masses

Photometric masses were derived by integrating the luminosity profiles for the disk and burst components and using their corresponding M/L values. The photometric masses were evaluated at radii taken from characteristics in the rotation curves (e.g. the last measured point or the radius of maximum velocity) to enable comparison with the kinematical mass estimates. In general, the luminosity profiles were integrated out to a radius corresponding to the last point in the rotation curve. In Table 3, we provide the photometric mass estimates, with their lower and upper limits. We also provide the dynamical mass estimate from Paper I, with the lower and upper limits (taking into account the uncertainty in inclination, the intrinsic dispersion, the uncertainty in the parameter f and the difference between different rotation curves or decomposition-models for the individual galaxies). In general, estimating the mass from the rotation curve will underestimate the dynamical mass since most likely these galaxies are not pure rotators. Random motions of the gas could provide significant dynamical support for our BCGs as indicated by their line widths (Table 4). For rotation curves with low amplitude and for the central regions, the contributions from velocity dispersion may dominate over the rotational component (however, see Sect 2.7).

For some galaxies there are several entries in Table 3. This may be the case e.g. when the rotation curve is not monotonously rising, or when there are several dynamical components. In those cases the rotational masses are derived for the relevant radius in question and the photometric mass is given for the same radius. For instance, for ESO 350-IG38 we present mass estimates for the last point in the rotation curve, for the maximum rotational velocity

and for the two components in the decomposed velocity field (see Paper I). In Fig. 2, the photometric and rotational mass estimates are compared (for reasons of clarity we plot only one point for each galaxy).

In all cases, except for one of the companions, the burst component dominates the optical luminosity (see Table 3). However, the integrated burst mass only makes up 2 to 5% of the total photometric mass. In Table 4, we give $M_{\text{ph},26}$, the photometric masses integrated out to the $\mu_V = 26$ mag/arcsec² isophote. This should be close to the total photometric masses, as the disk component outside these radii should contribute only on the order of one percent of the total mass if the M/L values are similar. In Table 4, we also present M/L_{26} , the global mass to light ratio, derived from $M_{\text{ph},26}$ and the integrated disk+burst light within the corresponding radius.

From Table 3 and Fig. 2 one sees that ESO 480-IG12 and ESO 338-IG04B are examples in which dark matter is needed within the extent of the rotation curves. In ESO 400-IG43B, Tololo 0341-403E and Tololo 0341-403W the photometric and rotational masses are in good agreement.

ESO 350-IG38, ESO 338-IG04, ESO 185-IG13 and ESO 400-IG43 present a deficit in the rotational mass estimates, as compared to the photometric mass. This result can be understood if the systems are not primarily rotationally supported or if the rotation curve does not reflect potential motions, either because the dynamics are not relaxed or if the H α emitting gas is not moving like the stars, even on a large scale. The latter is not so likely although the H α velocities are probably also affected by winds and expanding bubbles. To settle this definitely, the stellar velocity field must be compared with that of the ionised gas. The case of ESO 338-IG04 is a clear example of a non-relaxed system in which such a discrepancy between the two mass estimates does exist.

The photometric mass scales with h_{75}^{-2} , whereas the rotational mass (M_{rot}) scales as h_{75}^{-1} . Hence, the “mass deficiency” apparent in some galaxies gets worse with lowering of the Hubble constant from the adopted value of 75 km/s/Mpc.

2.7. Do the H α line widths trace mass?

Terlevich and Melnick (1981) showed that giant HII-regions display a positive correlation between radius, the H β luminosity and the H β emission line width. They have argued that this reflects an underlying mass relation and that the H β line width traces virial motions. This is somewhat surprising since one expects also other processes, such as SNe feedback, to contribute to the emission line widths. HII galaxies (galaxies with HII region like spectra, i.e. \sim BCGs) seems to follow the same relation, suggesting that they are scaled up versions of giant HII-regions (Melnick et al. 1987). This also makes it possible to use HII galaxies as standard candles to probe cosmological parameters like the H_0 and Λ (Melnick et al. 1988, 2000).

If the Balmer emission line widths indeed reflect virial motions, they may be used to derive the dynamical mass of a galaxy. In Table 4, we provide, $r_{e,d}$, the effective radii of the disk components and $\sigma_{\text{H}\alpha}$, the measured H α line-widths ($\sigma = FWHM/2.35$). The $\sigma_{\text{H}\alpha}$ values are the average line-widths where each pixel is weighted by its H α intensity. They were derived from the velocity dispersion maps² rather than from the integrated profiles. Hence the line widths given in Table 4 are not influenced by the overall rotation of the galaxies. The mass which can be supported by velocity dispersion, M_σ , was estimated from $M_\sigma = 3 \cdot 1.6 \cdot r_{e,d} \cdot \sigma^2 / G$, (Guzmán et al. 1996, Bender et al. 1992). With M_σ in M_\odot , $r_{e,d}$ in kpc, and σ in km/s, this becomes:

$$M_\sigma = 1.1 \cdot 10^6 \cdot r_{e,d} \cdot \sigma^2$$

We caution that this is a quite crude estimate, which assumes that the line width is due to virial motions in response to the gravitational potential of the underlying disk component. If the bursts are caused by infalling material, which is not virialised, this is not necessarily true. Since $r_{e,d}$ scales linearly with the inverse of h_{75} , so M_σ does as well.

The interesting point is that, for the galaxies which present a deficit in the rotational mass estimate, we can solve the mass discrepancy by invoking that these systems are supported by velocity dispersion instead of rotation. This can be seen by comparing M_σ and $M_{\text{ph},26}$ in Table 4. However, this does not solve the problem of why some of our galaxies have such strangely shaped rotation curves, e.g. rapidly declining, as for ESO 350-IG38 and ESO 400-IG43. In general, the mass discrepancies occur outside the centre, which dominates the measured line widths. The ultimate test of the importance of the underlying gravitational potential on the H α line widths would be to derive the stellar velocity dispersion. Kobulnicky and Gebhardt (2000) showed that the central velocity dispersion derived from stars and ionised gas in general agree in a sample of late type galaxies.

3. Dynamical mass models

Above and in Paper I, we used the rotation curves to construct simple integrated dynamical mass estimates, based on the formula given by Lequeux (1983). In this section we will briefly discuss more detailed mass models involving a dark matter halo, and which also take the radial behaviour of the luminosity profile and the rotation curve into account.

Given the luminosity profiles for the burst and disk components, and their associated M/L values (see Table

² Except for ESO 338-04, the $\sigma_{\text{H}\alpha}$ values given in Table 4 were derived from complimentary Fabry-Perot observations utilising an interferometer with large spectral range and were obtained at ESO/La Silla in September 1999 and 2000. For ESO 338-04 $\sigma_{\text{H}\alpha}$ is derived from the data presented in Fig. 7 in Paper I.

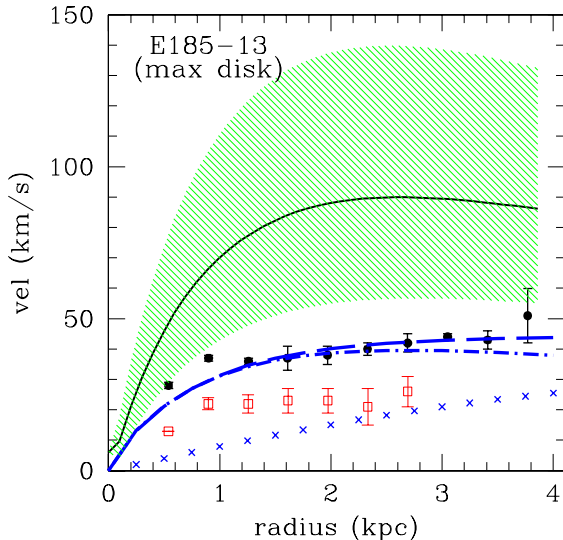


Fig. 4. Mass model for ESO 185-IG13 employing the “maximum disk” method. The main component of the rotation curve from the decomposed velocity field is shown as filled circles, and the secondary counter-rotating component is shown as open squares. The dynamical disk and halo components were fitted to the main component. For further explanations see caption of Fig. 3.

2), it is possible to predict what the rotation curve should look like, under the assumption that there is no dark matter. We call these *photometric rotation curves*. These photometric rotation curves are the minimum allowed velocities for rotational support. In Figs. 3 to 5, these are shown as full drawn lines with a hatched region for the allowed interval (given by the M/L intervals in Table 2). We show only the disk component, since the burst component in all cases gives a negligible contribution.

Dynamical mass models, based on the observed rotation curve and the observed shape of the disk and burst luminosity profiles, were also constructed. Again, the burst component gives a negligible contribution and for reasons of clarity we do not include it in the presented mass models.

The technique used to construct the mass models is described in Carignan & Freeman (1985) and the code we used was kindly provided to us by Claude Carignan. Both “maximum disk” and “best fit” approaches were undertaken. A χ^2 minimization technique is used in the three-parameter space of the model. These parameters are: The mass-to-light ratio of the stellar disc (M/L_{disk}^*), the core radius (r_{halo}) and the one-dimensional velocity dispersion (σ_{halo}) of the dark isothermal halo. The mass models are presented in Figs. 3 to 5: the dash-dot lines gives the disk component, the crosses give the halo component and the long dashed lines give the total disk+halo component. The latter should be compared with the observed rota-

tion curve which is shown as dots with errorbars (here the error bars reflect the discrepancy between the approaching and receding sides). In general we show the maximum disk models since they provide upper limits to the mass contained in stars.

When viewing Figs 3 to 5, the galaxies fall in two categories: Four of the galaxies (ESO 350-38, ESO 400-43, ESO 185-13 and ESO 338-04) have observed rotation curves that are well below the predicted photometric rotation curves. This was expected in view of the mass discrepancies discussed in Sect. 2.5. In ESO 350-38 and ESO 185-13 the shape of the rotation curve and the disk component of the mass model agree reasonably well when using the primary component of the decomposed velocity fields, but the observed rotation is too slow (marginally in ESO 185-13, significantly in ESO 350-38). ESO 185-13 could possibly be saved by adopting an IMF with a flat low mass part, if the dynamical mass has also been underestimated (e.g. by overestimating the inclination), but not ESO 350-38. For ESO 400-43 and ESO 338-04 it was even impossible to construct a mass model, due to the divergent shapes of the observed and photometric rotation curves.

In the other galaxies, there is no apparent deficiency of rotation. In ESO 480-12 and ESO 338-04B we see a significant contribution from a dark matter halo to the dynamics. In ESO 400-43B and Tololo 0341-407E there is marginal evidence for dark matter: the fit is improved by including a dark halo, but the luminous matter still dominates within the extent of the rotation curve. In Tololo 0341-407W we see no signature of a dark halo. In these 5 cases the disk components agree rather well with the photometric rotation curves.

The galaxy ESO 338-IG04B has both well behaved dynamics and photometric structure. For this galaxy, the maximum disk and best fit models give the same result: $M/L_{disk}^* = 4$, core radius of the dark halo $r_{halo} = 9$ kpc, and a halo velocity dispersion $\sigma_{halo} = 100$ km/s. The 99.9% confidence interval is $M/L_{disk}^* = 3.2$ to 4.8. The photometric estimate is $M/L_{disk} = 3.4$ with a 3 sigma confidence interval 2.5 to 6.0. A photometric mass slightly lower than the dynamical one is expected with the presence of an HI disk. Thus there is a very good agreement between the purely dynamical and the purely photometric M/L estimates, which give us confidence in our photometric M/L estimating procedure.

4. Discussion of individual objects

In this section, we discuss the kinematics and morphology of the individual targets. In addition, the velocity fields are thoroughly described in Paper I. For all galaxies we show isovelocity contours for the H α emitting gas, overlaid on broad band images. The labels of the isovelocity contours are given in Paper I.



Fig. 6. The $H\alpha$ iso-velocity contours overlaid on an R-band CCD image of ESO 350-IG38. The velocities to which the contours correspond can be found in Paper I. North is up, and east to the left. The size of the field is 1 by 1 arcminute, corresponding to 23×23 kpc. Note the irregular morphology at all isophotal levels. The faintest visible structures are $\mu_R \approx 26$ mag/arcsec².

4.1. ESO 350-IG38 (*Haro 11*)

This galaxy has a heart shaped morphology, with three bright starburst nuclei (Fig. 6). The outer morphology is distorted out to very faint isophotal levels (see Fig. 6 where the faintest visible structures are $\mu_R \approx 26$ mag/arcsec²). This is seen more clearly in broad bands than in $H\alpha$ demonstrating that the light originates mainly in stars. Hence, the large scale distribution of stars in this galaxy is highly asymmetric. At all isophotal levels an extension in the south-eastern direction is evident. This may be a tidal tail in development, or the remnants of a such. $H\alpha$ images reveal faint arms extending from the south-eastern and south-western nuclei. An HST/WFPC2 archive image reveals that the three very bright starburst nuclei at the center of ESO 350-IG38 are composed of numerous individual super-star clusters with luminosities up to $M_V = -15$. The total number of luminous star clusters is very high (Östlin 2000). Emission from the south-east nucleus is dominated by a resolved very high surface brightness “nucleus” with $M_V = -17.5$ with no apparent internal structure. The properties of these central regions bear a close resemblance to the classical colliding galaxies NGC 4038/4039 as seen in HST data (Whitmore and Schweizer 1995).

The $H\alpha$ line profiles of this galaxy are broad, up to FWHM=270 km/s, and have a non-gaussian shape. This suggests that two or more non-virialised components may be present. In the centre, double peaked lines are present

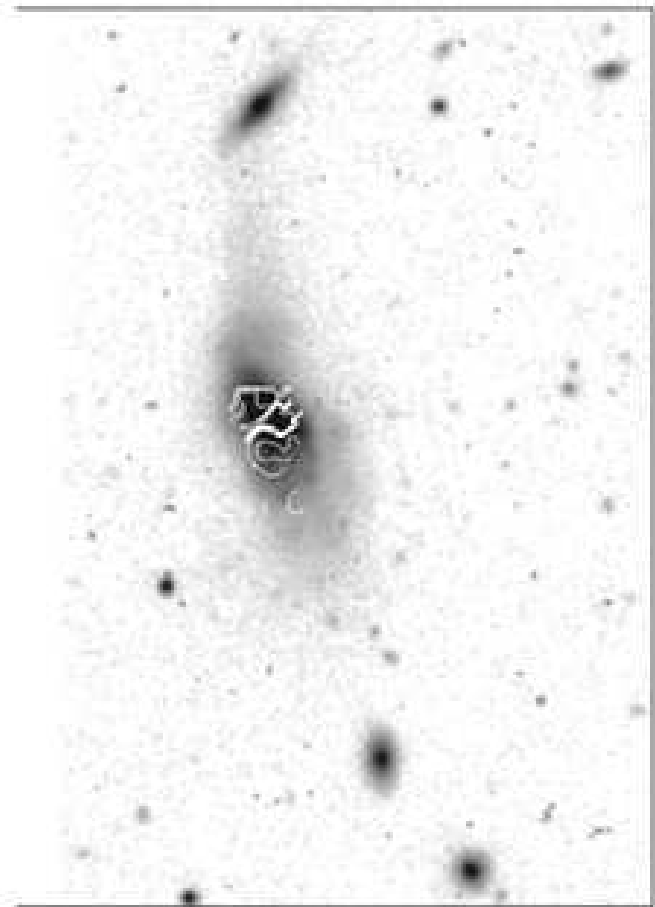


Fig. 7. The $H\alpha$ iso-velocity contours of the primary dynamical component in ESO 480-IG12 (see Paper I) overlaid on an R-band CCD image. North is up, and east to the left. The size of the field is 1.7 by 2.5 arcminutes, corresponding to 30×45 kpc.

consistent with the presence of a counter-rotating disk (see Fig. 3 and Paper I) or high velocity blobs. These properties indicate that the centre is not dynamically relaxed, while the outer velocity field shows a very slow rotation. The estimated stellar mass density exceeds by far what can be supported by the observed amount of rotation (≈ 30 km/s). Thus, the galaxy is either not in equilibrium, or it is not primarily supported by rotation. These properties strongly suggest that the starburst was triggered by a merger process.

This galaxy is the most massive in the whole sample and also has the highest star formation rate. The inferred (core-collapse) supernova frequency is one every 7 years. Surprisingly, it seems to be rather devoid of cool gas (Bergvall et al. 2000), suggesting that the starburst is about to run out of fuel.

4.2. ESO 480-IG12

An intriguing finding with this galaxy is that it has strong outer morphological distortions (Fig. 7) and that it is apparently aligned with a chain of galaxies in a background

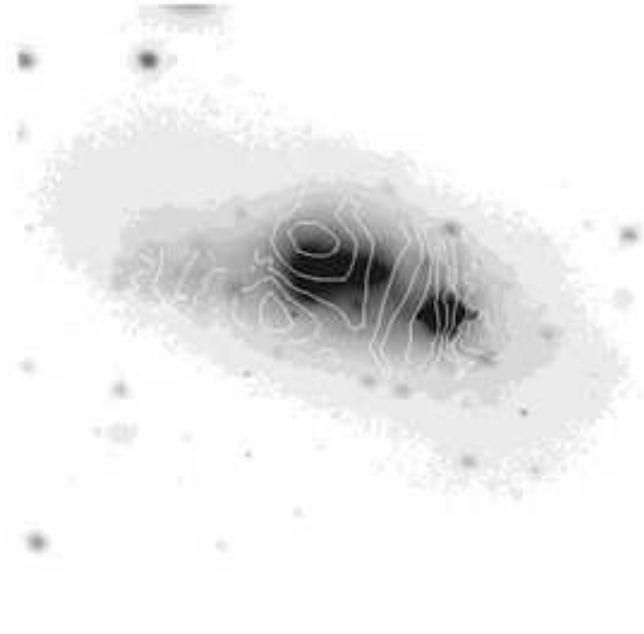


Fig. 8. The $H\alpha$ iso-velocity contours of ESO 338-IG04 overlaid on a R-band CCD image. North is up, and east to the left. The size of the field is $60'' \times 53''$, corresponding to 11×9.5 kpc.

(uncatalogued) cluster. Spectra have been obtained for three of the galaxies with the smallest angular distance from ESO 480-IG12, which however are at much higher red-shift (~ 30000 km/s), but it cannot be excluded that one of the galaxies apparently belonging to the cluster is in fact a low mass companion of ESO 480-IG12.

The northern extension is long and narrow while the south one is broader and more diffuse. South of the centre, there are several kiloparsec scale plumes. In addition, there are several small faint blobs in the southern part. High resolution images would reveal if these are extended or perhaps compact star clusters, like those seen in ESO 338-IG04, ESO 350-IG38 and ESO 185-IG13. The overall morphology presents large-scale asymmetries down to the faintest visible levels, compare e.g. the north and south-west extensions. This indicates an asymmetric and non-equilibrium distribution of stars, which may be due to an interaction/merger or a strong warp.

The velocity field is irregular with double line profiles, almost over the entire galaxy, and two components have successfully been fitted in Paper I. The double lines could arise in a separate dynamical component or an outflow or expanding super bubble. The rotation curve and luminosity distribution suggest that dark matter dominates the dynamics (see Fig. 3).

4.3. ESO 338-IG04 (*Tololo 1924-416*)

This well-known BCG has an almost chaotic velocity field, with strong gradients and an extended tail with little internal velocity structure (Fig. 8). It has a companion at a

projected distance of 70 kpc to the south-west (see next subsection). Approximately $10''$ east of the centre, just at the border of the central star-forming region, there is a velocity component whose kinematical axis is perpendicular to the photometric major axis of the galaxy (see Paper I). The radial light distribution indicates that the observed mean rotational velocity (if a such is at all meaningful to define in view of the irregular velocity field, see Fig. 3) cannot support the system gravitationally.

There is a 5 kpc long tail towards the east, and large scale isophotal asymmetries down to the 26 mag/arcsec^2 level. At fainter levels the morphology becomes more regular, but a box-like shape remains on the western side. The tail has much bluer colours than the rest of the galaxy outside the starburst region, signifying a younger stellar population. It contains stellar clusters, and cannot be explained by a purely gaseous tail. The tail has almost no velocity gradient with respect to the centre ($\Delta v \leq 10$ km/s). On the other hand, the western half of the galaxy has a strong gradient and an implied rotational velocity of 80 km/s at a distance of 3 kpc from the centre (Fig. 5 in Paper I). This is identical to the rotational velocity in the companion ESO 338-IG04B which has an equal photometric mass. Hence, the western part of the galaxy shows about the expected level of velocity difference with respect to the centre for rotational support to be possible. But what is happening at the eastern side in the tail? The colour of the tail suggest that it has a distinctly different stellar population from the rest of the galaxy. The most likely is that the tail is a remnant of a merger and that projection effects prevent us from seeing the true velocity amplitude. The parts of the galaxy on the eastern side which are not in the tail, do not emit in $H\alpha$, hence we have no information on its kinematics. Where the tail meets the starburst region we see an increased $H\alpha$ velocity dispersion, perhaps due to a shock. This coincides with the location of the perpendicular dynamical component discussed above. The companion is probably too far away for tidal forces to have caused the starburst and peculiar velocity field.

Radio interferometric observations (Östlin et al. in preparation) reveal that the galaxy is embedded in a very large HI cloud, more than 7 arcminutes across (corresponding to 80 kpc at the distance of ESO 338-IG04). The HI cloud has irregular morphology with two main components and no single axis of rotation. ESO 338-IG04 appears to be located in the eastern HI cloud. The morphology and velocity field of the HI complex is consistent with a close interaction/merger of two gas-rich galaxies or HI clouds. The companion (see next subsection) is detected in HI but lies further away.

Although we cannot exclude that the starburst in ESO 338-IG04 is triggered by interaction with the companion, a merger appears more likely in view of the complex velocity field and the non-rotating arm. HST observations of this well known starburst has revealed that in addition to many young compact star clusters, it contains a system of intermediate age (~ 2 Gyr) globular clusters

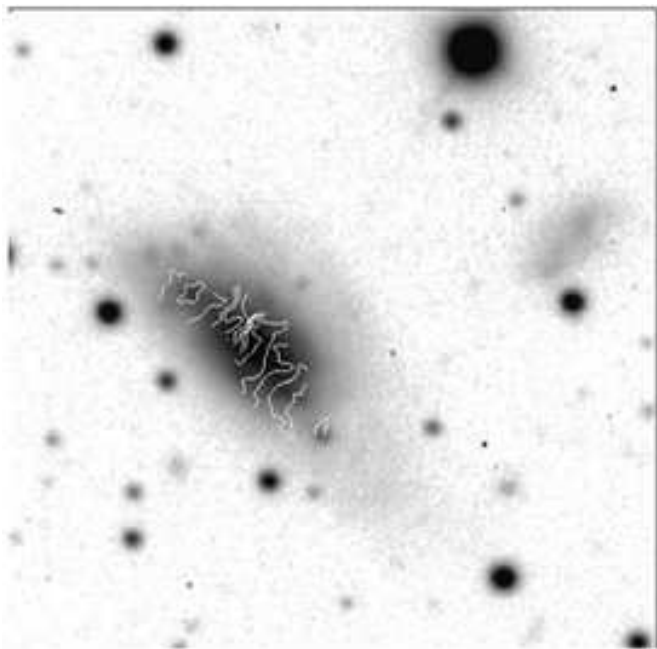


Fig. 9. The $H\alpha$ iso-velocity contours of ESO 338-IG04B overlaid on an V-band CCD image. North is up, and east to the left. The size of the field is $83'' \times 83''$, corresponding to 15×15 kpc. Note the low surface brightness galaxy north-west of ESO 338-IG04B

(Östlin et al. 1998), a fossil of a previous dramatic starburst event.

4.4. ESO 338-IG04B (companion)

This is a physical companion to ESO 338-IG04. The projected distance between the galaxies is 70 kpc. Although the colours are fairly blue, ESO 338-IG04B is not a BCG, and the star formation rate is moderate and does not imply a starburst (see Table 4). Photometry indicates an old underlying stellar population (Bergvall and Östlin 2000). The star formation in this galaxy could have been enhanced by the tidal drag from ESO 338-IG04, but the velocity field is regular and apparently unperturbed (Fig. 9). The kinematics of this galaxy support the presence of a dark matter halo (see Fig. 3). The stellar mass of this galaxy is of the same order as that of ESO 338-IG04, but the estimated SFRs differ by more than a factor of ten. North-west of the galaxy a low surface brightness galaxy is detected in broad band images, but not in the Fabry-Perot $H\alpha$ images, hence its distance is unknown.

4.5. ESO 185-IG13

ESO 185-IG13 presents a clear example of classical morphological perturbations produced in galaxy mergers and/or collisions (Barnes and Hernquist 1992; Schweizer 1998). The broad band images of this galaxy (see fig. 10) clearly reveal the presence of a tidal tail $30''$ long in the

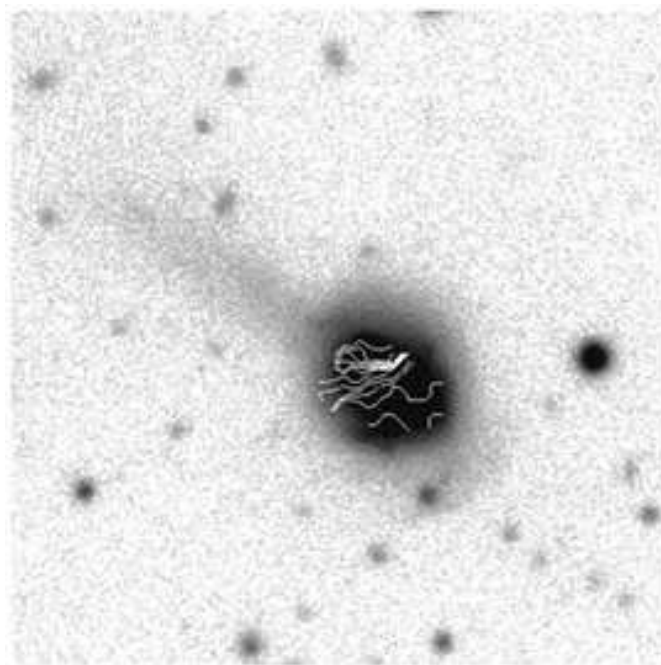


Fig. 10. The $H\alpha$ iso-velocity contours of the primary dynamical component of ESO 185-IG13 overlaid on a V-band CCD image. North is up, and east to the left. The size of the field is $50'' \times 50''$ corresponding to 18×18 kpc.

north-east direction (about 10 kpc at the distance of the galaxy main body).

On CCD images, there are two small faint galaxies with fairly low surface brightness approximately 1.5 arcminutes south-west of ESO 185-IG13. None of these were detected in the Fabry-Perot data, hence their distances are unknown. An HST image of ESO 185-IG13 (obtained from the archive) reveals the presence of numerous compact star clusters with luminosities up to $M_V \approx -15$ (Östlin 2000), a typical signature of colliding system (see Whitmore et al. 1993, 1995). Most of the bright cluster sources are concentrated to a central bar like structure. Both the HST and ground based images reveal the presence of arms in the center, though with no counterpart in the Fabry-Perot $H\alpha$ image or velocity field.

The analysis of the velocity field of ESO 185-IG13 revealed the presence of two dynamically distinct components (Paper I). The secondary component is counter-rotating with respect to the main component (which spins faster and dominates the $H\alpha$ emission). The two components have marginally different position angles. If the two components represent gas discs that intersect, this configuration cannot be long lived (the rotation period of the secondary component is $\approx 4 \times 10^8$ years). Despite a regular rotation curve, the observed level of rotation cannot support the observed photometric mass (see Fig. 4). However, given the limited surface photometry available, and the lack of near-IR data, the estimated M/L for the disk component is rather uncertain. If the IMF has a flat low mass part (see Sect 2.4) and if we have underestimated

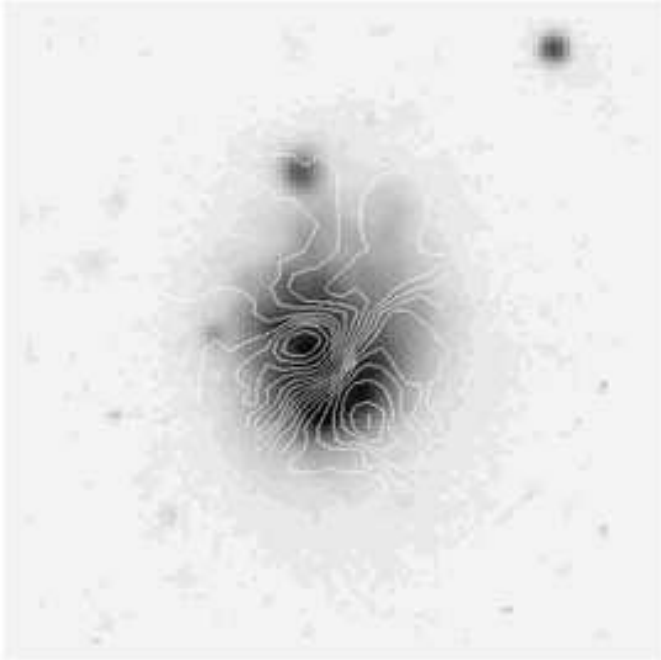


Fig. 11. The $H\alpha$ iso-velocity contours of ESO 400-G43 overlaid on an R-band CCD image. The grey scale has been chosen to show detail rather than depth. North is up, and east to the left. The size of the field is $50'' \times 50''$, corresponding to 19×19 kpc. The source $15''$ north of the centre is an $H\alpha$ emitting region at the red-shift of ESO 400-G43.

the amount of rotation (e.g. due to projection effects) and take into account the sum of the two components (as in Fig. 2), it might be possible to solve the mass discrepancy. In summary, this is a clear example of a BCG where the starburst has been triggered by a merger.

4.6. ESO 400-G43

This galaxy has a regular outer morphology, embedded in a large HI cloud that is extended towards a companion galaxy with a projected distance of 70 kpc (Bergvall and Jörsäter 1988, see next subsection). At fainter isophotal levels peculiar morphological features start to appear. Approximately $15''$ north of the centre there is a bright $H\alpha$ emitting blob, apparently not rotating with the galaxy at the pattern speed expected at its location.

The rotation curve shows a rapid increase followed by a dramatic decline, that drops faster than the keplerian prediction (see Fig. 5 and Paper I). This is obviously unphysical for an equilibrium disc. A possible interpretation is that the cause of the super-keplerian rotation speed is infall towards the centre. A $B - R$ image of ESO 400-G43 shows a shell-like structure with radius ~ 1.5 to 3 kpc. This may be a sign of superbubbles or stellar resonances, like the “shells” found in many merger remnants. In the north-west, starting $10''$ from center, there are signs of an arm/plume both in the velocity field and broad band images (Fig. 11). Our kinematical data for the ionised gas

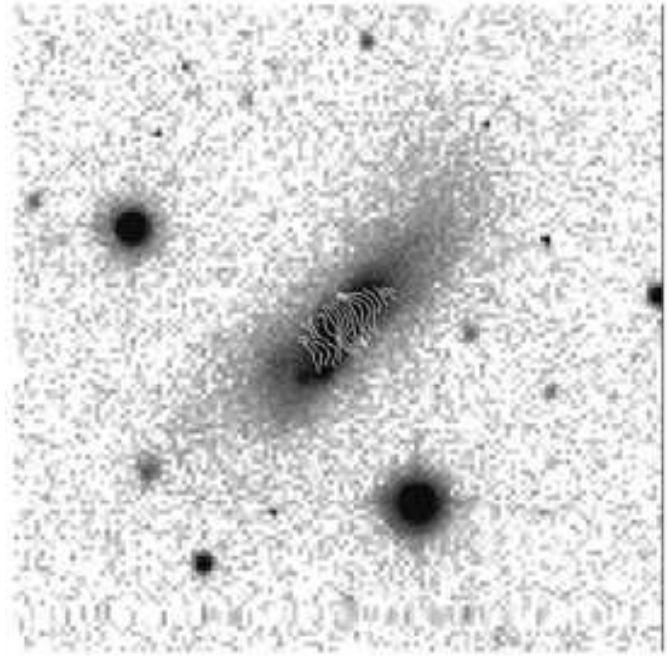


Fig. 12. The $H\alpha$ iso-velocity contours of ESO 400-G43B overlaid on an R-band CCD image. North is up, and east to the left. The size of the field is 1 by 1 arcminute, corresponding to 22×22 kpc.

is in good agreement with the results by Bergvall and Jörsäter (1988). The published HI kinematical data show a rotation curve with a rotational velocity of ~ 50 km/s (Bergvall and Jörsäter 1988), i.e. similar to the central value in the $H\alpha$ rotation curve before the super keplerian decline. Bergvall and Jörsäter (1988) suggested that this galaxy was a genuinely young galaxy and that the super-keplerian drop was due to a non-relaxed disk. The latter conclusion remains likely, although it is evident that the galaxy contains an old underlying population (Bergvall and Östlin 2000). It is likely that a rapid infall of gas towards the center is fuel for the starburst but – what gave rise to the infall? The most efficient infall mechanisms are bar instabilities and mergers, but there are no signs of a bar in ESO 400-G43. The northern bright HII region might be an infalling blob, or something that has just plunged through the HI disc. Slightly more than an arcminute to the north-east there is a positive detection of a massive HI cloud, which may be interacting with ESO 400-G43 (Bergvall and Jörsäter 1988).

The low rotational velocity outside the centre cannot, by far, support the stellar mass gravitationally (Figs 2 and 5). The observed $H\alpha$ line widths (see Table 4) could be sufficient for gravitational support if the linewidth traces virial motions. However, this can not explain the observed shape of the rotation curve. Clearly, this galaxy is badly perturbed dynamically. The only likely explanation is interaction with the companion ESO 400-G43B or that a merger with a smaller galaxy has occurred.

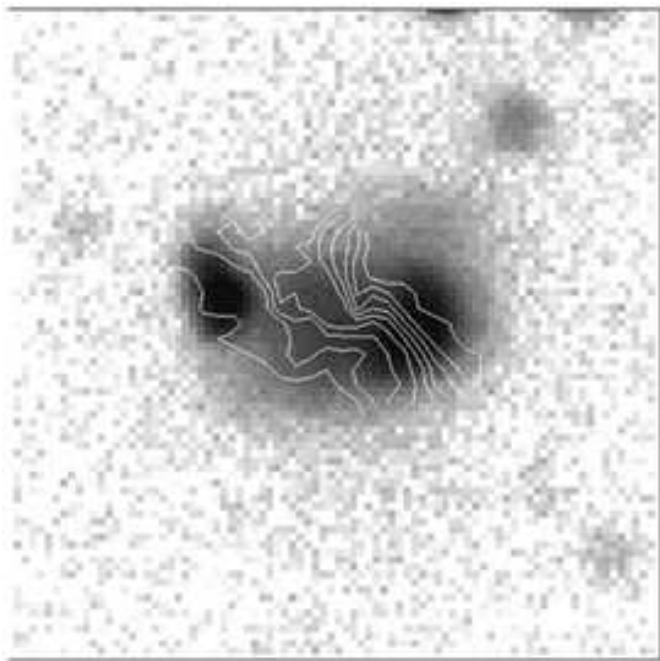


Fig. 13. The $H\alpha$ iso-velocity contours of Tololo 0341-407 overlaid on an R-band CCD image. North is up, and east to the left. The size of the field is $37'' \times 37''$, corresponding to 11×11 kpc.

4.7. ESO 400-G43B (companion)

This physical companion to ESO 400-G43 (Bergvall and Jörsäter 1988) is a regular dwarf galaxy with a regular rotation curve (Figs. 5 and 12). The shape of the rotation curve does not follow the light distribution which indicates the presence of a dark matter halo (Fig. 5). The properties of ESO 400-G43B are fairly similar to those of ESO 338-IG04B, but it has more intense star formation activity. The time scales for gas consumption and buildup of the observed stellar mass are both on the order of 3-4 Gyr. Thus, this galaxy is at the limit of being classified as a starburst galaxy. The star formation occurs in a central extended HII region. It is quite probable that interaction with ESO 400-G43 increased the star formation activity.

4.8. Tololo 0341-407

This galaxy is the faintest BCG in the sample. It has two apparent nuclei embedded in an irregular envelope (Fig. 13). The velocity field shows the two nuclei to belong to distinct dynamical systems. In Paper I we successfully decomposed this galaxy into two dynamical components coinciding with the optical components on the broad band image. This may be two dwarf galaxies currently coming together. The eastern component (Tololo 0341-407E) has a very high SFR per unit mass, whereas Tololo 0341-407W is similar to the more luminous BCGs in this respect. Notice that both galaxies are far less massive than the other galaxies in the sample.

This is the only galaxy in the sample for which we do not have multi-colour CCD photometry, hence we could not determine M/L . As an estimate for M/L we took the median for the other galaxies, and for $M/L_{\text{disk}}^{\text{min}}$ and $M/L_{\text{disk}}^{\text{max}}$ we used the extreme values of the distribution for the other galaxies. Hence, the mass estimates for this system are more uncertain than for the other galaxies. Nevertheless, the maximum disk solutions are close to the predicted photometric rotation curves, and in the Eastern component we see marginal evidence for a dark matter halo (Fig. 5).

5. Discussion

5.1. Energetic feedback from star formation

Supernova (SN) explosions and winds from massive stars provide input of mechanical energy into the ISM in galaxies. In a starburst, the collective action of many supernovae may lead to a galactic wind, transporting material out from the plane of the galaxy. Winds could affect the velocity field of the ionised gas and has to be taken into account. Observationally, winds have been seen in some low luminosity, hence low mass, BCGs (Meurer et al. 1992, Papaderos et al. 1994, Lequeux et al. 1995, Martin 1998).

Recent models which include also the restoring force provided by dark matter have shown that feedback from star formation is not expected to cause gas loss from galaxies more massive than $10^8 M_{\odot}$ (MacLow and Ferrara 1999, Ferrara and Tolstoy 2000). Thus for the galaxies studied in this paper, it should be safe to conclude that feedback has not affected the global velocity fields. However, the calculations by MacLow and Ferrara (1999) and Ferrara and Tolstoy (2000) are restricted to energy injection rates corresponding to supernova frequencies of one SN every 30 000 years or less. In this sample, where the derived star formation rates span the range 0.25 to $20 M_{\odot}/\text{year}$, we expect (assuming a Salpeter IMF with $M_{\text{low}} = 0.1$, $M_{\text{up}} = 100 M_{\odot}$, and lower initial mass limit for core-collapse supernova of $8 M_{\odot}$) SN frequencies of 0.02 to 0.15 SN/year, hence 3 orders of magnitude larger! Extrapolating the calculations by MacLow and Ferrara we still do not expect blow-away to occur, while blow-out is possible. Of course, extrapolating by 3 orders of magnitude is dubious. If gas gets blown out, it will stay in the halo and may later condense back on the host galaxy.

Interestingly, deep $H\alpha$ images of ESO 338-IG04 and ESO 350-IG38 show that the $H\alpha$ morphologies are extended along the minor axis, compared to the broad band morphologies. This is what is expected for disk galaxies: gas escapes perpendicular to the plane while the gas in the plane is little affected. Thus the rotation curves, which are derived along the major axis, are probably not affected by outflows and expanding superbubbles while the velocity fields along the minor axis may well be (e.g. in ESO480-IG12).

5.2. Morphology

Our sample of relatively luminous BCGs have irregular morphology at both bright and faint isophotal levels. This agrees with the findings of Telles et al. (1997) that BCGs with irregular morphology at faint isophotal levels are on average more luminous than those with regular morphology.

A galaxy in equilibrium should have a regular symmetric morphology and kinematics. The occurrence of star formation, if not symmetrically distributed, may create apparent morphological irregularity. Nevertheless, the outer parts of a galaxy are essentially unaffected by the central activity, hence the outer isophotes of a galaxy mainly trace the distribution of stars. Therefore, significant large scale asymmetries in the outer isophotes are signatures of an asymmetric distribution of stars. Such asymmetries could be the consequence of an interaction/merger but weaker distortions could also be produced by instabilities which may be inherent or tidally triggered. Mergers and interactions between galaxies lead to large scale morphological distortions (e.g. tidal tails and shells) and to perturbations in their rotation curves due to gas flows driven into the center. The light distributions of the 6 BCGs presented in this study show outer distortions to some extent which may suggest that the starbursts have been produced by interactions or mergers. In some cases, like ESO 185-IG13 and ESO 350-IG38, the merger signatures are very strong.

In principle, one of the best ways to investigate the effect of interaction between galaxies should be through the kinematics of the gas, since it traces well the dynamics of the burst tidally triggered through the collision of gas-rich systems. From the reported results we have shown that on the top of a slow rotating disk system, important dynamical perturbations have been detected which prevent us in some cases from obtaining the gravitational mass of the galaxies. None of the BCGs show regular disk kinematics and different explanations have to be invoked for each particular case (see Sect. 3 and 4). It has to be noticed that the only truly regular kinematics occur in the companion galaxies or when we can disentangle quite well the different kinematical components, as in the cases of ESO 185-IG13, ESO 480-IG12 and Tololo 0341-403. It is then not surprising that we cannot define a general trend for all the studied galaxies. Depending on the state in which we see the interaction/merger, we will detect more or less chaotic velocity maps.

5.3. Environmental aspects

Most investigations of the environments of BCGs have shown that these kind of galaxies are rather isolated with respect to giant luminous galaxies and preferentially occupy low and intermediate density environments (see Introduction). We have used NED³ to investigate the environment of the galaxies in this study. Since NED was

mainly composed from catalogues of bright galaxies, such a study essentially provides information on the presence of massive neighbouring galaxies. We searched a projected radius of 1 Mpc around the galaxies, and ± 1000 km/s in velocity space. The velocity range was chosen very generously so as not to reject possible neighbours with high peculiar velocities. Travelling one Mpc with a velocity of 1000 km/s would take one Gyr. Thus, if galaxies so far apart have ever interacted, this must have happened more than 1 Gyr ago, even for very high peculiar velocities. Hence, any signs of interaction (e.g. a triggered starburst) should be long gone. None of the galaxies in this study has any neighbour in NED within 1 Mpc, except for ESO 338-IG04 and ESO 400-G43, the companions of which are included in this study.

The analysis shows that the local density of catalogued galaxies is not enhanced in the locations where these galaxies are found; typically we find a density of catalogued galaxies of 0.005 Mpc^{-3} , when averaged over a volume 2500 Mpc^3 or greater. Thus, the sample studied is not located in particularly dense environments. In general, galaxy evolution is a strong function of the density of the environment. In low red-shift clusters, interactions are frequent but rarely lead to any significant star formation. The most active star-forming galaxies and star-forming mergers are found in the field or in sparse groups, and this is true also for BCGs, luminous or not.

5.4. The ignition of a starburst

A fundamental astrophysical problem is how to ignite a starburst. The majority of galaxies are not involved in starbursts. For example, low surface brightness galaxies (LSBGs) have very low star formation rates, despite the generous supply of HI, which may be explained by sub-critical HI column densities (van der Hulst et al. 1993). Efficient star formation requires gas with high densities. Here we consider as starbursts, galaxies which have gas depletion time-scales, and time-scales for accumulating the observed photometric mass with the current SFR much shorter than a Hubble-time, i.e. $\tau_{\text{ph}} \sim 1$ Gyr or less.

A model where starbursts in dwarf galaxies are the consequence of statistical fluctuations was presented by Gerola et al. (1980). Their model predicts that for galaxies with radii less than 1-2 kpc, star formation will principally occur in short bursts, whereas larger galaxies are predicted to have more continuous star formation. A similar argument is that only when the star formation in a single giant molecular cloud would exceed the time averaged SFR in a galaxy would we expect statistical fluctuations to dominate. Hence for galaxies with a baryonic mass greater than $10^8 M_{\odot}$, statistical fluctuations should not dominate the global SFR. The galaxies presented in this paper are too large/massive for any significant statistical fluctuations to be expected.

A popular scenario for BCGs has been one with cyclic bursts. Here, the starburst is terminated by the expulsion

³ NASA/IPAC Extragalactic Database

of gas through supernova winds. If the gas later accretes back to the galaxy, a new starburst could be ignited. A potential problem is, however, the time-scale for the retrieval of the gas. If the blown out gas eventually accretes back on the galaxy, one expects this to occur over a time-scale much longer than the duration of a starburst. A constant inflow of gas at a slow rate is not likely to produce a starburst, unless there is some threshold mechanism. But even if there is a threshold, the accreted gas mass has to pass it coevally. Since the star formation efficiency is less than 100%, the gas accretion rate must be higher than the SFR. Such a high continuous mass accretion rate would not be compatible with the total gas+star masses of the galaxies. For our BCGs which have burst masses of $10^8 M_\odot$ or larger, on the order of a few times 10^8 to $10^9 M_\odot$ of gas would have to pass the threshold within a few times 10^7 years. This implies a mass accretion time scale of the same order as the free fall time. Hence, gas falling back would have to come all at once in one lump, contrary to the expected continuous accretion. One could of course envision that the expelled gas cools and clump together in a few giant massive HI complexes, and if such an aggregation would fall into the centre, we could get a starburst. The time-scale for building up the observed photometric mass with the current SFR is $\tau_{\text{ph}} \sim 1$ Gyr (see Table 4), which indicates that if the burst duration is ≤ 100 Myr, the duty cycle between bursts should be on the order of 1 Gyr. We would thus require that gas is ejected on time scales shorter than 100 Myr, then the gas should stay away for 1 Gyr, and finally, most of it should fall back within some 10 Myrs. Supernova activity will begin after a few Myrs, whereas the bursts we observe in these BCGs have already been active for several 10 Myrs. Hence, although we in some cases see signatures of expanding bubbles, we see no evidence for any superwinds capable of blowing out the ISM and terminating star formation. Because of these arguments, we do not consider a self-regulated cyclic starburst scenario very likely for these luminous BCGs. A cyclical burst scenario, powered by winds or stochastic effects, is more likely in low mass BCGs.

Tidal forces generate gas flows that could funnel gas at large radii into the center of a galaxy and ignite a starburst, but generally on time scales that are too long to build up high central densities in competition with the destruction processes of molecular cloud complexes. Campos-Aguilar et al. (1993) showed that a dwarf galaxy is sensitive to tidal triggering only when the companion galaxy is very massive. With the lack of massive companions, interactions will only be strong when two dwarfs are actually merging or in physical contact. Similarly, Icke (1985) found that separations between galaxies for tidal gas flows to occur must be within a few galactic radii, but the typical time-scale is of the order of a galactic rotation period (here a few 100 Myrs). Thus, a weak tidal gas flow might well increase the star formation rate but likely not ignite a starburst. Mihos et al. (1997) used N-body simulations to study the response of LSBGs (possible progenitors of BCGs) to tidal interactions. They found

that due to the low mass densities, LSBGs are very stable against tidal triggering, in contrast to normal high surface brightness giant disc galaxies. As there are no massive galaxies in the vicinity of our studied BCGs, and the two known companions are rather distant (more than 70 kpc), tidal interactions cannot be the main cause of the starbursts. However, tidal interactions may be responsible for the moderately high SFRs seen in the two companions.

Another scenario for BCGs is that the starburst is ignited through the merging between two dwarfs, or between a dwarf and a massive intergalactic gas cloud. In a merger, gas clouds lose a considerably fraction of their angular momentum in dissipative collisions and fall into the center of the galaxy/galaxies. The time-scale is sufficiently short for building up large overdensities that can start to form stars coevally. This is thus an attractive scenario for the origin of starbursts in BCGs. Massive isolated HI clouds seem to be very rare at the current epoch (see Kunth and Östlin 2000). However, any merger involving a sufficiently gas-rich component could do the job. Mergers involving at least one gas-rich component is the mechanism favoured for the BCGs in this sample.

HST observations of ESO 338-IG04 has revealed that it contains a rich population of young globular clusters (Östlin et al 1998). Similar rich populations of luminous star clusters were found in HST archive images of ESO 350-IG38 and ESO 185-IG13 (Östlin 2000). Numerous young globular cluster candidates have also been found in mergers, like the "Antennae" and NGC 7252 (Whitmore et al. 1993, 1995), and galactic bars (e.g. Barth et al. 1995). In the latter case, the star cluster formation probably is triggered by resonances enhancing the gas density. With respect to the host galaxy luminosity, luminous BCGs like ESO 338-IG04, ESO 350-IG38 and ESO 185-IG13 contain higher numbers of compact star clusters than the classical mergers (Östlin 2000). A nearly coeval formation of a hundred globular clusters requires the build up of massive dense gas clouds on a time-scale of a few 10 Myrs. In dwarfs, where resonances that could help build-up large overdensities, are absent, mergers may be the only way to create the necessary conditions for cluster formation to occur in great numbers (see e.g. Elmegreen and Efremov 1997). Hence the richness of young massive star clusters in three of our galaxies is another support for the merger origin of their starbursts.

5.5. Relations to other galaxy types

Given that the high SFRs seen in these luminous BCGs are transient, one might ask what came before, and what will follow: in between the burst phases a BCG will have a very different appearance. It is however hazardous to draw any general conclusions about the BCG phenomenon from such a small sample of luminous BCGs. The morphological diversity, notably the existence of BCGs with regular vs irregular outer envelopes, suggests the possi-

bility that different types of BCGs may have a different origin (Kunth and Östlin 2000).

The possible evolutionary links between BCGs and other types of galaxies have been widely discussed in the literature (see e.g. Davies and Phillips 1988; Dekel and Silk 1986; Lin and Faber 1983; Thuan 1992; Babul and Rees 1992; Papaderos et al. 1996; Bergvall et al. 1998,1999; Kunth and Östlin 2000). For the luminous BCGs in this study, a merger origin is favoured for most of the galaxies. The merger should include at least one gas-rich dwarf or alternatively massive intergalactic HI-cloud. This suggests that at least one dwarf irregular or LSBG is involved. LSBGs may be the most common type of galaxy in the universe, thus providing plenty of fuel for BCG activity. Mergers between spirals are believed to produce elliptical galaxies. Since several of our galaxies seem to rotate too slowly, one might speculate that they will evolve into low mass elliptical galaxies. However, to answer the question about the fate of these BCGs, information on stellar dynamics is required.

Studies of faint galaxies, e.g. in the Hubble Deep Field (HDF), has revealed the presence of a population of high red-shift ($z = 0.4$ to 1.4) compact emission line galaxies (Phillips et al. 1997), which may be responsible for up to 45% of the global cosmic SFR at $0.4 < z < 1.0$ (Guzmán et al. 1997). Comparing the mass averaged SFRs, line widths, line ratios etc, of our local BCGs to those derived for the compact galaxies in the HDF (Guzmán et al. 1997), we find them to have very similar properties, in particular when compared to the high ($z > 0.7$) red-shift subsample. Glazebrook et al. (1995,1998) identified the excess of faint blue galaxies in deep galaxy counts with peculiar/interacting galaxies, and showed that such galaxies are blue, compact and actively star-forming, with typical luminosities $M_B = -19$, i.e. very similar to the galaxies discussed in this paper. In hierarchical galaxy formation scenarios, massive galaxies are successively built up by galaxies of lower mass. Le Fèvre et al. (2000) show that mergers play a major role in galaxy evolution also at $z < 1$. Thus, the local luminous BCGs may be the present day equivalents (NB not counterparts) of high red-shift BCGs and faint blue galaxies. The study of local luminous BCGs offers insights to the mechanisms operating at higher red-shifts and offers a way of studying hierarchical buildup in action.

6. Summary and conclusions

We present the results from the most extensive study as yet of optical 2D velocity fields of luminous blue compact galaxies (BCGs) utilising Fabry-Perot interferometry, targeting the H α emission line. The velocity fields and rotation curves for a sample of six luminous BCGs and two companions were presented in a previous paper (Östlin et al. 1999, Paper I). The velocity fields present large scale peculiarities, and secondary dynamical components (e.g. counter-rotation) are common.

In this paper we have analysed the ionised gas dynamics together with optical/near-infrared surface photometry and spectral synthesis models to constrain the dynamical and photometric masses of the galaxies. Moreover, we construct multi-component mass models including a dark halo component.

The BCGs in this study are starbursts in the sense that the time-scale for building up the observed stellar mass with the current star formation rate, derived from the H α luminosities, is much smaller than a Hubble time. We find that the young burst population dominates the integrated optical luminosities, while only contributing 1 to 5% of the total stellar mass, which ranges from a few times 10^8 to more than $10^{10} M_\odot$. The mass is dominated by an older underlying population and the integrated (burst + old population) mass-to-light ratios are $M/L_V \sim 1$.

In about half the cases, the observed rotational velocities are too small to allow for pure rotational support. A possible explanation is that velocity dispersion dominates the gravitational support. This is consistent with the observed line widths ($\sigma_{H\alpha} = 35$ to 80 km/s), but does not explain the strange shape of many of the rotation curves. Another possibility is that the galaxies are not in dynamical equilibrium, e.g. because they are involved in mergers, explaining the peculiar kinematics. It is also possible that gas and stars are dynamically decoupled and the H α velocity field does not trace the gravitational potential. A way to distinguish between these alternatives would be to obtain the rotation curve and velocity dispersion for the stellar component. In two cases, we find evidence for the presence of dark matter within the extent of the H α rotation curves, and in two other cases we find marginal evidence.

We have further analysed the morphology of the BCGs, and in general we find strong large-scale asymmetries down to the faintest isophotal levels, revealing large scale asymmetries in the distribution of stars. In most cases we see clear signatures of merging/interaction.

We have discussed the possible trigger mechanisms for the strong starbursts in this sample of luminous BCGs. When considering also the kinematics and morphologies we are lead to the conclusion that dwarf galaxy mergers is the favoured explanation for the starbursts. The two companion galaxies appear largely unaffected by the presence of their brilliant neighbours, but their star formation activity may have increased due to the tidal drag imposed by the BCGs. The dynamics of the studied galaxies fall in two broad classes: one with well-behaving rotation curves at large radii and one with very perturbed dynamics. This may indicate a distinction of the fate of these galaxies, once the starbursts fade. Alternatively, depending on the state in which we see the interaction/merger, we will detect more or less chaotic velocity fields. These local dwarf galaxy mergers may be the best analogues of hierarchical buildup of more massive galaxies at high red-shifts.

In 1999 and 2000 new Fabry-Perot observations were obtained for another 15 BCGs, extending down to fainter luminosities. Together with the present data set, we will

have high quality velocity fields for two dozen BCGs. This will allow us to obtain a more comprehensive picture of the evolution of BCGs.

Acknowledgements. Thanks to Torgny Karlsson for reducing a CCD image of ESO185-IG13, and to Ernst van Groningen for obtaining additional data on this galaxy. Thanks also to Mats Dahlgren for obtaining the CCD image of Tololo0341-407. Claude Carignan is thanked for fruitful discussions on the dynamics of BCGs and for making specific adaptations of his mass model code for the present study. Albert Bosma is thanked for stimulating discussions on the interpretation of velocity fields. Anna Westman is thanked for her great help in preparing the figures. An anonymous referee is thanked for many useful comments on the manuscript. G. Östlin acknowledges financial support from the Swedish Foundation for International Cooperation in Research and Higher Education (STINT). This work was partly supported by the Swedish Natural Science Research Council. This work is based on observations collected at the European Southern Observatory La Silla, Chile.

References

- Babul A., Rees M., 1992, MNRAS 255, 346
 Barnes, J.E., Hernquist, L. 1992, Nature 360, 715
 Barth A.J., Ho L.C., Fillipenko A.V., Sargent W.L., 1995, AJ 110, 1009
 Bender R., Burstein D., Faber S.M., 1992, ApJ 399, 462
 Bergvall N., Jörsäter S. 1988, Nat 331, 589
 Bergvall N., Olofsson K., 1986, A&AS, 64, 469
 Bergvall N., Östlin G. 2001, submitted to A&A
 Bergvall N., Rönnback J., 1995, MNRAS 273, 603
 Bergvall N., Östlin G., Pharasyn A., Rönnback J., Masegosa J., 1999, Highlights in astronomy Vol. 11A (Kluwer), p. 103
 Bergvall N., Östlin G., Masegosa J., Zakrisson E., 1999, Ap&SS 269, 625
 Bergvall N., Masegosa J., Östlin G., Cernicharo, J., 2000, A&A 359, 41
 Calzetti D., Kinney A.L., Storchi-Bergmann T., 1994, ApJ 429, 582
 Campos-Aguilar A., Moles M., Masegosa J., 1993, AJ 106, 1784
 Carignan, C., Freeman, K.C., 1985, Ap. J. 294, 494
 Castellani V., Chieffi A., Pulone L., 1991, ApJS 76, 911
 Cowie L., Songaila A., Hu E., 1991, Nat 354, 460
 Davies J.I., Phillipps S., 1988, MNRAS 233, 553
 Dekel A., Silk J., 1986, ApJ 303, 39
 Doublier V., Caulet A., Comte G., 1999, A&AS 138, 213
 Elmegreen B.G., Efremov Y., 1997, ApJ 480, 235
 Fanelli M.N., O'Connell R.W., Thuan T.X., 1988, ApJ 334, 665
 Ferland G.J., 1993, University of Kentucky Departments of Physics
 Ferrara A., Tolstoy E., 2000, MNRAS 313, 291
 Fioc M., Rocca-Volmerange B., 1999, astro-ph/9912179
 Gerola H., Seiden P.E., Schulman L.S., 1980, ApJ 242, 517
 Gil de Paz A., Zamorano J., Gallego J., 1999, MNRAS, 306, 975
 Glazebrook K., Ellis R.S., Santiago B., Griffiths R., 1995, MNRAS 275, L19
 Glazebrook K., Abraham R., Santiago B., Ellis R.S., Griffiths R., 1998, MNRAS 297, 885
 Guzmán R., Koo D.C., Faber S.M., Illingworth G.D., Takamiya M., R.G. Kron, Bershady M., 1996, ApJ 460, L5
 Guzmán R., Gallego J., Koo D.C., Phillips A.C., Lowenthal J.D., Faber S.M., Illingworth G.D., Vogt N.P., 1997, ApJ 489, 599
 Icke V., 1985, A&A 144, 115
 Iovino A., Melnick J., Shaver P., 1988, ApJ 330, L17
 Izotov Y., Thuan T.X., 1999, ApJ, 511, 639
 Kroupa P., Tout C.A., Gilmore G., 1993, MNRAS 262, 545
 Kunth D., Östlin G., 1999, A&AR 10, 1
 Kunth D., Sargent W.L.W., 1983 ApJ 273, 81
 Kunth D., Maurogordato S., Vigroux L., 1988 A&A 204, 10
 Kurucz R.L., 1992, in Barbuy B., Renzini A., eds, Proc IAU Symp. 149
 Lacey C., and Silk J., 1991, ApJ 381,14
 Le Fèvre O., Abraham R., Lilly S.J., Ellis R.S., Brinchmann J., Schade D., Tresse L., Colless M., Crampton D., Glazebrook K., Hammer F., Broadhurst T., 2000, MNRAS, 311, 565
 Lequeux J., 1983, A&A 125, 394
 Lequeux J., Peimbert M., Rayo J.F., Serrano A., Torres-Peimbert S., 1979, A&A 80, 155
 Lequeux J., Kunth D., Mas-Hesse J.M, Sargent W.L.W., 1995, A&A 301, 18
 Loose, H.-H., and Thuan T.X., 1985, in Star-forming dwarf galaxies and related objects, eds. Kunth D., Thuan T.X. , and Tran Thanh Van J., Edition Frontieres, Gif sur Yvette, p. 73
 Lin D., Faber S., 1983, ApJ 266, L21
 MacLow M.-M., Ferrara A., 1999, ApJ 513, 142
 Marlowe A., Heckman T., Wyse R., Schommer R., 1995, ApJ 438, 563
 Martin C., 1998, ApJ 506, 222
 Mas-Hesse J.M., Kunth D., 1999, A&A 349, 765
 Masegosa J., Moles M., Campos-Aguilar A., 1994, ApJ 420, 576
 Melnick J., Moles M., Terlevich R., Garcia-Pelayo J.-M., 1987, MNRAS 226, 849
 Melnick J., Terlevich R., Moles M., 1988, MNRAS 235, 297
 Melnick J., Terlevich R., Terlevich E., 2000, MNRAS 311, 629
 Meurer G.R., Freeman K.C., Dopita M.A., Cacciari C., 1992, AJ 103, 60
 Meurer G.R., Carignan C., Beaulieu S., Freeman K.C., 1996, AJ 111, 1551
 Meurer G.R., Staveley-Smith L., Killeen N.E.B., 1998, MNRAS 300, 705
 Mihos J.C., McGaugh S.S., de Blok W.J.G., 1997, ApJ 477, L79
 Miller, G. E.; Scalo, J. M.. 1979, ApJS 41, 513
 Östlin G., Bergvall N., 1994, in ESO/OHP workshop on dwarf galaxies, eds. Meylan G., and Pruginel P., ESO Conference and Workshop Proceedings No. 49, p. 451
 Östlin G., Bergvall N., Rönnback J., 1996, in The Interplay Between Massive Star Formation, The ISM and Galaxy Evolution, eds Kunth D., Guiderdoni B., Heydari-Malayeri M., and Thuan T.X., Edition Frontieres, p. 605
 Östlin G., Amram P., Masegosa J., Bergvall N., Boulesteix J., 1999, A&AS 137, 419
 Östlin G., Bergvall N., Rönnback J., 1998, A&A 335, 85
 Östlin G., in "Massive Stellar Clusters", A. Lancon and C. Boily Eds., ASP Conf. Ser. 211, p. 63
 Papaderos P., Fricke K.J., Thuan T.X., Loose H.-H., 1994, A&A 291, 13
 Papaderos P., Loose H.-H., Fricke K.J., Thuan T.X., 1996, A&A 314, 59

- Phillips A.C., Guzmán R., Gallego J., Koo D.C., Lowenthal J.D., Vogt N.P., Faber S.M., Illingworth G.D., 1997, *ApJ* 489, 543
- Petrosian A.R., Boulesteix J., Comte G., Kunth D., LeCoarer E., 1997, *A&A* 318, 390
- Salpeter E.E., 1955, *ApJ* 121, 161
- Salzer J.J., 1989, *ApJ* 347, 152
- Salzer J.J., MacAlpine G.M., Boroson T.A., 1989, *ApJS* 70, 479
- Sargent W., Searle L., 1970, *ApJ* 162, L155
- Scalo J.M., 1986, *FCPh* 11,1
- Scalo J.M., 1998, *ASP Conf. Ser.* 142, p. 201
- Schaller G., Schaerer D., Meynet G., Maeder A., 1992, *A&AS* 96, 269
- Searle L., Sargent W., 1972, *ApJ* 173, 25
- Searle L., Sargent W.L.W., Bagnuolo W.G., 1973, *ApJ* 179, 427
- Schweizer, F. 1998, in *Galaxies: Interactions and Induced Star Formation*, Saas-Fee Advanced Course 26. Edited by D. Friedli, L. Martinet, and D. Pfenniger (Springer-Verlag Berlin), p. 105
- Taylor C.L., 1997, *ApJ* 480, 524
- Taylor C.L., Brinks E., Grashuis R.M., Skillman E.D., 1995, *ApJS* 99, 427
- Taylor C.L., Brinks E., Grashuis R.M., Skillman E.D., 1996a, *ApJS* 102, 189 (erratum)
- Taylor C.L., Thomas D.L., Brinks E., Skillman E., 1996b, *ApJS* 107, 143
- Telles E., Maddox S., 2000, *MNRAS* 311, 307
- Telles E., Terlevich R., 1995, *MNRAS*, 275, 1
- Telles E., Terlevich R., 1997, *MNRAS*, 286, 183
- Telles E., Melnick J., Terlevich R., 1997, *MNRAS* 288, 78
- Terlevich R., Melnick J., 1981, *MNRAS* 195, 839
- Terlevich R., Melnick J., Masegosa J., Moles M., Copetti M., 1991, *A&AS* 91, 285
- Thuan T.X., 1992, in *Physics of nearby galaxies, nature or nurture?*, XXVIIth Recontres de Moriond, Eds. Thuan T.X., Balkowski C., Tran Thanh Van J., Edition Frontieres, Gif Sur Yvette, p. 151
- Thuan T.X. Williams T.B. and Malmuth E. 1987, in *Starbursts and Galaxy Evolution XXIIId Recontres de Moriond*, Eds. Thuan T.X. Montmerle T., Tran Thanh Van J., Edition Frontieres, Gif Sur Yvette, p. 225
- VandenBerg D., 1985, *ApJS* 58, 711
- van der Hulst J.M., Skillman E.D., Smith T.R., Bothun G.D., McGaugh S.S., de Blok W.J.G., 1993, *AJ* 106, 548
- van Zee L., Skillman E.D., Salzer J., 1998c, *AJ* 116, 1186
- Whitmore B., Schweizer F., 1995, *AJ* 109, 960
- Whitmore B., Schweizer F., Leitherer C., Borne K., Robert C., 1993, *AJ* 106,1354

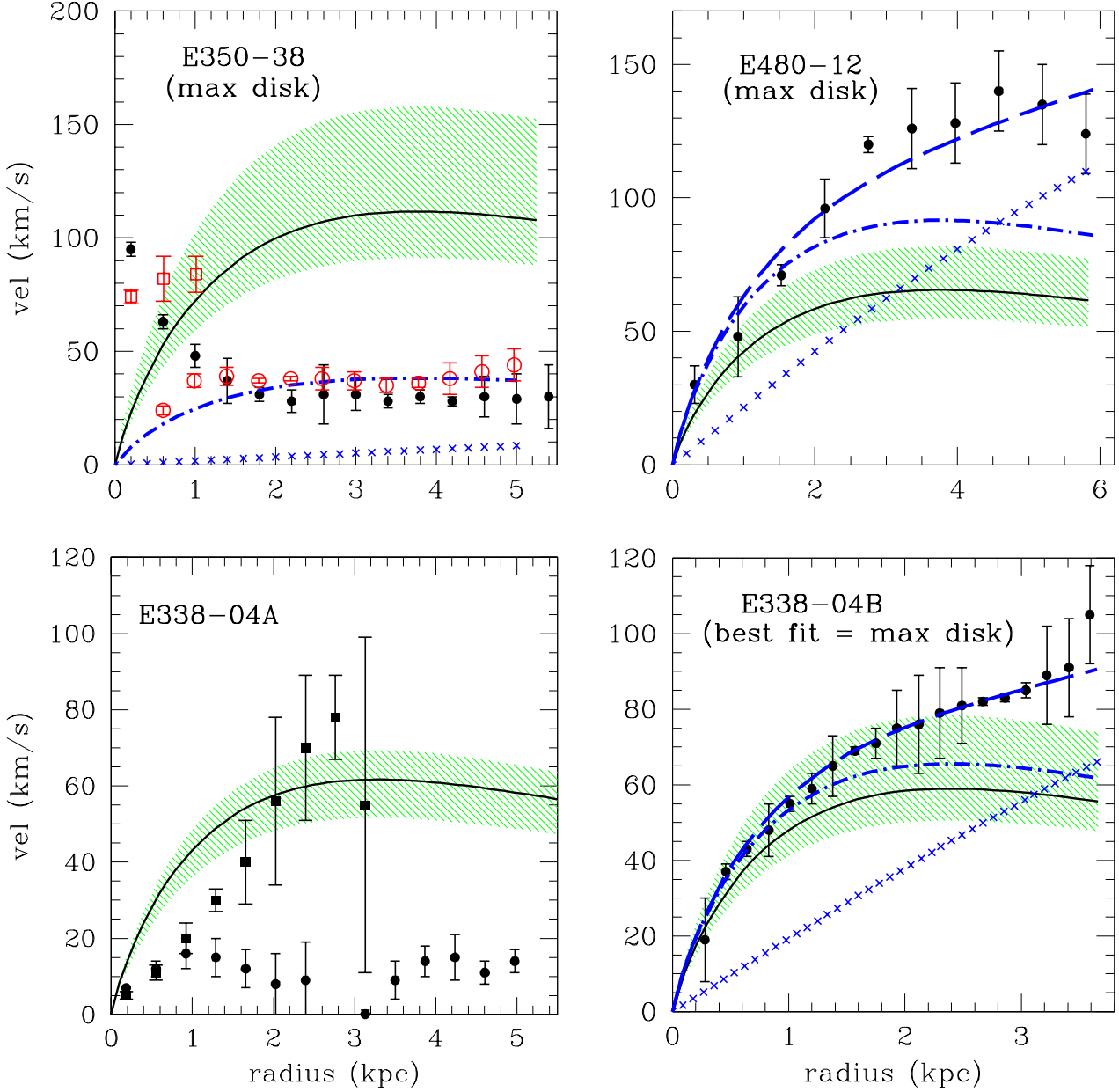


Fig. 3. Mass models for ESO 350-IG38, ESO 480-IG12, ESO 338-IG04 and ESO 338-IG04B. The filled circles with error bars show the observed rotation curves (see Paper I). The solid line is the photometric rotation curve for the disk component; and the shaded area is the allowed range based on the uncertainty in M/L . The dash-dot line is the stellar disk component from the mass model and the crosses are the halo component; the total model (disk+halo) is shown by the thick long dashed line (only for those cases where the halo component is non-zero). For ESO 350-IG38, the rotation curve resulting from the non-decomposed velocity field is shown as filled circles. The main component of the rotation curve for the decomposed velocity field is shown as open circles, and the secondary counter-rotating component is shown as open squares. The dynamical mass model was fitted to the main component of the decomposed velocity field. For ESO 338-IG04, the receding side of the rotation curve is shown as filled circles and the approaching side as filled squares. No disk and halo component are shown since it was impossible to construct a dynamical mass model.

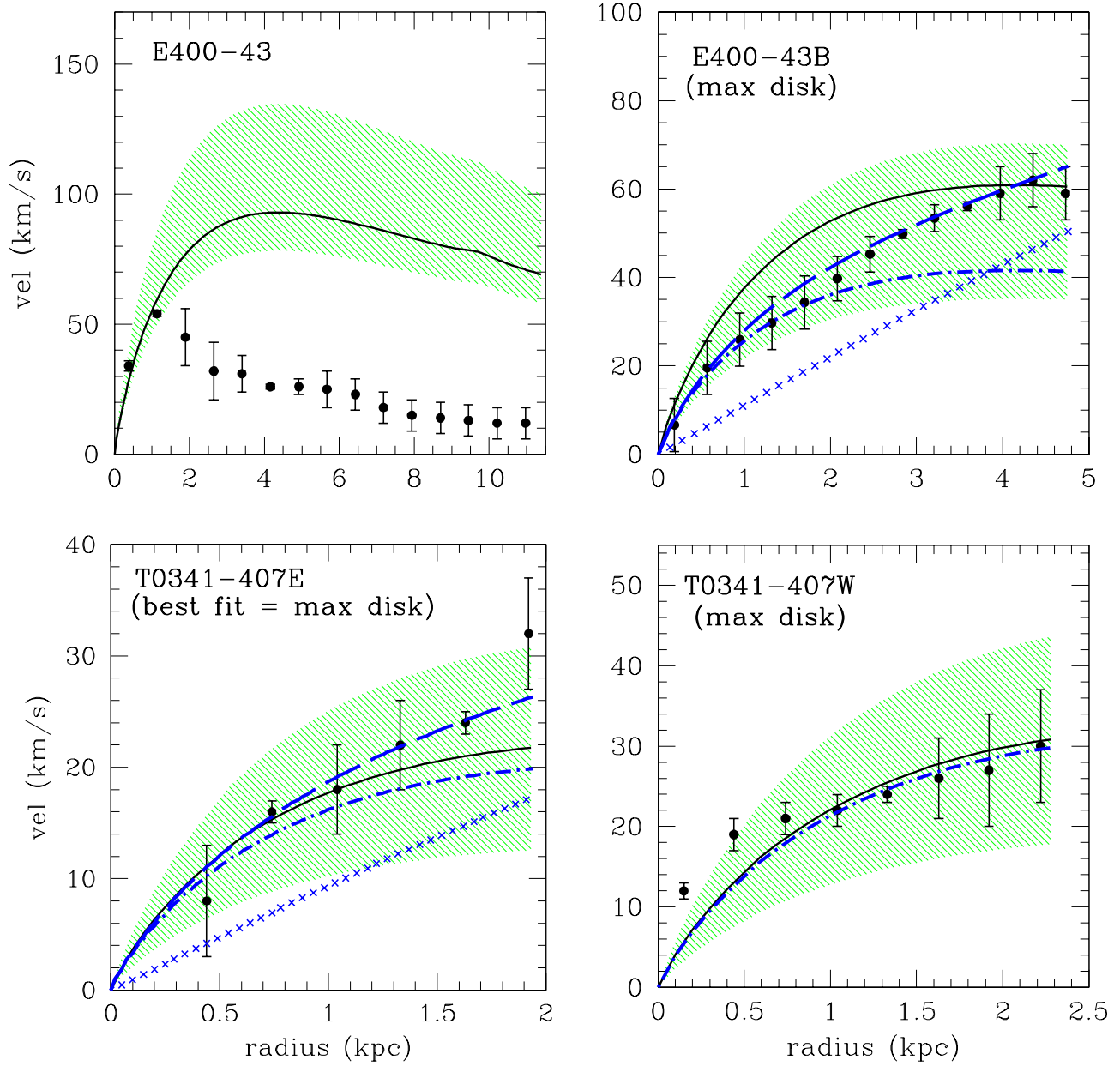


Fig. 5. Mass model for ESO 400-G43, ESO 400-G43B, Tololo0341-407E and Tololo0341-407W. For further explanations see caption of Fig. 3. For ESO 400-G43 no disk and halo component are shown since it was impossible to construct a dynamical mass model.